Southern Ocean Circulation and Eddy Compensation in CMIP5 Models

STEPHANIE M. DOWNES AND ANDREW MCC. HOGG

Research School of Earth Sciences, and ARC Centre of Excellence for Climate System Science,
The Australian National University, Acton, Australian Capital Territory, Australia

(Manuscript received 24 July 2012, in final form 6 March 2013)

ABSTRACT

Thirteen state-of-the-art climate models from phase 5 of the Coupled Model Intercomparison Project (CMIP5) are used to evaluate the response of the Antarctic Circumpolar Current (ACC) transport and Southern Ocean meridional overturning circulation to surface wind stress and buoyancy changes. Understanding how these flows—fundamental players in the global distribution of heat, gases, and nutrients—respond to climate change is currently a widely debated issue among oceanographers. Here, the authors analyze the circulation responses of these coarse-resolution coupled models to surface fluxes. Under a future CMIP5 climate pathway where the equivalent atmospheric CO_2 reaches 1370 ppm by 2100, the models robustly project reduced Southern Ocean density in the upper 2000 m accompanied by strengthened stratification. Despite an overall increase in overlying wind stress (~20%), the projected ACC transports lie within ±15% of their historical state, and no significant relationship with changes in the magnitude or position of the wind stress is identified. The models indicate that a weakening of ACC transport at the end of the twenty-first century is correlated with a strong increase in the surface heat and freshwater fluxes in the ACC region. In contrast, the surface heat gain across the ACC region and the wind-driven surface transports are significantly correlated with an increased upper and decreased lower Eulerian-mean meridional overturning circulation. The change in the eddy-induced overturning in both the depth and density spaces is quantified, and it is found that the CMIP5 models project partial eddy compensation of the upper and lower overturning cells.

1. Introduction

The complex and eddy-rich Southern Ocean circulation drives the interbasin exchange of heat, salt, gases, and nutrients, and its variability is a crucial component of global climate change (Sabine et al. 2004; Le Quéré et al. 2007). The Antarctic Circumpolar Current (ACC) flows quasi zonally around the entire Southern Ocean between approximately 45° and 65°S. The ACC is driven by a combination of surface buoyancy and momentum fluxes and limited largely by topographic interaction (Rintoul et al. 2001). The ACC extends vertically to almost the ocean floor and (in a zonally averaged framework) is associated with two major meridional overturning circulation (MOC) cells, namely upper and lower (cf. Speer et al. 2000). The upper cell describes the upwelling of southward-flowing deep waters and the equatorward return flow of lighter mode and intermediate waters. The lower cell combines the densest part of the southward-flowing deep waters with newly formed northward-flowing bottom waters originating along the Antarctic continental shelf. Two currently outstanding issues in the oceanography community are 1) how surface wind and buoyancy forcing will influence the ACC transport and the upper and lower MOC cells in a changing climate, and 2) the role played by ocean mesoscale eddies in moderating changes in the circulation. Here, we utilize several global climate models forced by the same anthropogenic emission scenario to investigate the response of the Southern Ocean's large-scale circulation to varying surface fluxes.

Two key, but not completely understood, concepts that describe the circulation's response to wind forcing are *eddy saturation* and *eddy compensation*. Eddy saturation is derived from the theoretical prediction that the net ACC transport may become insensitive to wind stress at sufficiently high stress (e.g., Straub 1993; Hallberg and Gnanadesikan 2006; Farneti et al. 2010). In this study, we evaluate the relative importance of winds, local

---

Corresponding author address: Stephanie Downes, Research School of Earth Sciences, The Australian National University, Acton ACT 0200, Australia.
E-mail: stephanie.downes@anu.edu.au

DOI: 10.1175/JCLI-D-12-00504.1

density fluxes, and eddies in controlling the response of the ACC transport to future climate change scenarios in the 13 coupled climate models.

The upper and lower overturning cells can be divided into Eulerian and eddy components, which counteract each other to produce the net or residual circulation. Eddy compensation refers to the competing effects of Ekman transports (i.e., the Eulerian component) and the opposing eddy-induced circulation (e.g., Marshall and Radko 2003; Viebahn and Eden 2010). Here, we investigate this theoretical prediction in 8 of the 13 assessed models. Even though the ACC transport is dynamically linked with the isopycnal slope and the MOC, the role of the winds and buoyancy in varying these circulation regimes differ. Eddies act throughout most of the water column, whereas the Eulerian-mean overturning is confined to the upper ocean and below the shallowest topography (Meredith et al. 2012; Morrison and Hogg 2013).

If eddy processes are an important component of Earth's response to climate change, then it is a matter of urgency to determine how well the coarse-resolution (~1° grid) oceans currently employed by climate models can represent them. For example, Farneti et al. (2010) compared a coarse- and high-resolution response to a doubling in strength and poleward shift in the westerlies and found that the ACC and MOC are substantially less sensitive to wind forcing in the higher-resolution climate model. In their ocean-only models, Munday et al. (2013) find that the ACC approaches complete saturation at high resolution, and Hallberg and Gnanadesikan (2006) find large differences in the ACC transport response for coarse versus eddy-permitting and eddy-resolving resolutions. Based on these results alone, one might well expect coupled climate models would overestimate the sensitivity to wind stress changes, particularly for ACC transport.

There is evidence to support the notion that both the ACC and MOC are sensitive to surface buoyancy forcing as well as wind stress (Borowski et al. 2002; Hogg 2010; Morrison et al. 2011; Shakespeare and Hogg 2012). Several multimodel analyses from phase 3 of the Climate Model Intercomparison Project (CMIP3)/Intergovernmental Panel on Climate Change Fourth Assessment Report (IPCC AR4) have assessed the influence of varying winds and buoyancy (heat and freshwater) fluxes on the Southern Ocean circulation. In these studies, the climate models suggest intensification and a poleward shift of the westerlies are associated with poleward shifts in the subtropical and subpolar gyres and ACC fronts, ocean warming, and increased upwelling and downwelling branches of the upper cell (Fyfe and Saenko 2006; Wang et al. 2011; Downes et al. 2010; Sen Gupta et al. 2009). However, contrary to the expectations from ocean-only model simulations, changes in the transport of the ACC in CMIP3 class models are not associated with the wind stress changes (e.g., Sen Gupta et al. 2009). The models project a weakening of the lower cell, though associated changes in surface fluxes are uncertain. This may be associated with an inability of models to correctly simulate polar processes associated with Antarctic Bottom Water formation (e.g., Downes et al. 2011). Using 13 phase 5 of the Coupled Model Intercomparison Project (CMIP5) models, we will deduce whether changes in the ACC transport under global warming are due to eddies opposing winds or due to changes in surface buoyancy input.

The above CMIP3 model studies have not associated their wind, buoyancy, and circulation findings with either the Eulerian or eddy MOC changes in the ocean interior but postulate the importance of considering the eddy-induced transports. The CMIP3 effort did not include the eddy-induced transport as an optional output field. The CMIP5 (Taylor et al. 2012) models have a key advantage in the quest to improve our understanding of physical processes driving changes in circulation as they can explicitly distinguish overturning due to the Eulerian-mean circulation versus that induced by (parameterized) eddies. Presently just a handful of the 40+ CMIP5 models have included the mean and eddy circulations in depth (and some in density) space in their output fields. We will quantify the compensation of the eddy MOC to the Eulerian MOC changes under the same climate forcing in eight CMIP5 models.

In the following section, we describe the main features of the 13 models and the observationally based estimates to which the models are compared. Our results are divided into three sections. The first is an investigation of the sensitivity of the ACC to future climate trends at the end of the twentieth and twenty-first centuries. We then analyze the Eulerian and eddy MOC in depth (eight models) and density (four models) space and finally analyze the sensitivity to wind and buoyancy forcing in density space. A summary and discussion of our main results includes comparisons of individual models with similar model components and an outline of possible influences of choice of model and model drift on our main results. To conclude, we condense our main results and provide insights and suggestions for future Southern Ocean multimodel circulation modeling.

2. Models and methods

a. The CMIP5 models

The 13 CMIP5 models chosen for our study (listed in Table 1 with full model expansions and model numbers)

TABLE 1. CMIP models used in this study and full expansions. Listed are the modeling institution and climate model (name used within this study) and its reference, atmosphere, and ocean components and ocean grid resolution for longitude (x), latitude (y), and number of depth levels (z). Note that in some models the latitude grid increases resolution toward the equator and hence a range is provided. The eight models used in the depth–space MOC analysis are indicated by an asterisk; a double asterisk is for models with MOC output analyzed in depth and density spaces. Model acronyms: UM = Unified Model; MOM4p1 = Modular Ocean Model, version 4p1; NEMO = Nucleus for European Modelling of the Ocean; AM2/3 = Atmospheric Model, version 2/3; MRI-AGCM3 = MRI Atmospheric General Circulation Model, version 3; MRI.COM3 = MRI Community Ocean Model, version 3; OGCM4 = Ocean General Circulation Model, version 4; ECHAM5/6 = European Centre for Medium-Range Weather Forecasts Hamburg Model, version 5/6; MPI-OM = Max Plank Institute Ocean Model; GOLD = Generalized Ocean Layer Dynamics; SAMIL2 = Spectral Atmospheric Circulation Model of IAP LASG, version 2; LICOM = LASG IAP Climate Ocean Model; ATM = Atmosphere Model; and POP2 = Parallel Ocean Program, version 2.

No.	Institution and model	Reference	Atmosphere	Ocean	Resolution (x°/y°/z m)
1	CAWCR Australian Community Climate and Earth-System Simulator, version 1.0 (ACCESS1.0)**	Bi et al. (2013)	UM (HadGEM2)	MOM4p1	1/⅓–1/50
2	CAWCR Australian Community Climate and Earth-System Simulator, version 1.3 (ACCESS1.3)**	Bi et al. (2013)	UM (HadGEM3)	MOM4p1	1/⅓–1/50
3	Commonwealth Scientific and Industrial Research Organisation Mark, version 3.6 (CSIRO Mk3.6)*	Rotstayn et al. (2012)	atmosphere–ocean coupled general circulation model (AOGCM)	MOM2.2	1.8/0.9/31
4	Centre National de Recherches Météorologiques Coupled Global Climate Model, version 5.1 (CNRM-CM5.1)	Voldoire et al. (2013)	Action de Recherche Petite Echelle Grande Echelle (ARPEGE-Climat v5.2)	NEMO(v3.2)	1/⅓–1/42
5	NOAA/GFDL Earth System Model with MOM4 ocean component (ESM2M) (GFDL ESM2M)**	Dunne et al. (2012)	AM2	MOM4p1	1/⅓–1/50
6	MRI Coupled Atmosphere–Ocean General Circulation Model, version 3 (CGCM3)	Yukimoto et al. (2012)	MRI atmospheric general circulation models version 3 (MRI-AGCM3)	MRI.COM3	1/0.5/50
7	CCCma Second Generation Canadian Earth System Model (CanESM2)**	Chylek et al. (2011)	atmospheric general circulation models version 4 (AGCM4)	OGCM4	1.41/0.94/40
8	Goddard Institute for Space Studies Model E2, coupled with Russell ocean model (GISS-E2-R)	Schmidt et al. (2006)	Model E	Russell	1.25/1/32
9	Max Planck Institute Earth System Model, low resolution (MPI-ESM-LR)	Jungclaus et al. (2012, manuscript submitted to *J. Adv. Model. Earth Syst.*)	ECHAM5/6	MPI-OM	1.5/1.5/40
10	Geophysical Fluid Dynamics Laboratory Earth System Model with GOLD ocean component (ESM2G) (GFDL ESM2G)	Dunne et al. (2012)	AM2	GOLD	1/⅓–1/50
11	GFDL Climate Model, version 3 (GFDL CM3)*	Griffies et al. (2011)	AM3	MOM4p1	1/⅓–1/50
12	LASG IAP Flexible Global Ocean–Atmosphere–Land System Model gridpoint, second spectral version (FGOALS-s2)*	Bao et al. (2013)	SAMIL2	LICOM	1/0.5–1/30
13	NCAR Community Climate System Model, version 4 (CCSM4)*	Gent et al. (2011)	ATM	POP2	1.125/0.25–0.5/60

are the Centre for Australian Weather and Climate Research (CAWCR) ACCESS1.0 and ACCESS1.3, CSIRO Mk3.6, CNRM-CM5.1, the National Oceanic and Atmospheric Administration (NOAA)/Geophysical Fluid Dynamics Laboratory (GFDL) ESM2M and ESM2G, the Meteorological Research Institute (MRI) CGCM3, the Canadian Centre for Climate Modelling and Analysis (CCCma) CanESM2, GISS-E2-R, MPI-ESM-LR, the

NOAA/GFDL CM3, the State Key Laboratory of Numerical Modeling for Atmospheric Sciences and Geophysical Fluid Dynamics, Institute of Atmospheric Physics (LASG IAP) FGOALS-s2, and the National Center for Atmospheric Research (NCAR) CCSM4. Our results can be expanded further as more model output becomes available; however, we argue that 13 models are sufficient for this study.

All these CMIP5 models have coarse resolution (i.e., ~1° horizontal grid spacing), except for NCAR-CCSM4 (½°) with a refined meridional resolution toward the equator in half the models. The CMIP5 models supersede the CMIP3 models via, for example, improved ocean and atmosphere physics and chemistry (e.g., radiative fluxes, energy budgets, interactive aerosol schemes, and eddy parameterizations) and the addition of an interactive carbon cycle in the formulation of the Earth System Model (CanESM2, ESM2M, ESM2G, and MPI-ESM-LR). The number of depth levels varies between 30 and 60, a marked increase for many of the models since the CMIP3 effort. The ACCESS, ESM2M, and CM3 models use z^* coordinates where the depth levels vary in time to allow for more flexible resolution near the free surface (Bi and Marsland 2010; Griffies 2007). Ocean model drift in variables such as temperature and sea level pressure have also been reduced (e.g., CNRM-CM5, CSIRO Mk3.6, and MRI-CGCM3). Some of the CMIP5 models now also include parameterizations such as tidally driven mixing (e.g., CanESM2, ESM2M, ESM2G, and MRI-CGCM3) and geothermal heating (e.g., CNRM-CM5, ESM2M, and ESM2G). We refer the reader to the references listed in Table 1 for a more comprehensive guide to, and evaluation of, individual models.

The models all use some form of the Gent and McWilliams (1990) mixing scheme to parameterize the eddy-induced streamfunction, where the eddy diffusivity κ ranges spatially between 10 and 1500 $\mathrm{m^2\,s^{-1}}$. Most of the models include a slope tapering coefficient (to deal with a large neutral slope near surface boundary layers) of between 0.001 and 0.02; the exception is in the isopycnic model ESM2G where bulk mixed layers exist near the surface. The CCSM4 model uses an eddy diffusivity that varies with space and time, ranging up to 3000 $\mathrm{m^2\,s^{-1}}$. Given the small number of models assessed here and the varying configurations of the eddy parameterizations, we do not link the parameterization with changes in the ACC or MOC transports. However, we note that Kuhlbrodt et al. (2012) concluded that models with a higher-constant (or at most varying with respect to latitude) Gent and McWilliams (1990) eddy diffusivity coefficient were significantly correlated with a weaker ACC transport.

CAWCR has developed two models with essentially identical oceans [Modular Ocean Model, version 4p1 (MOM4p1); Griffies 2007] and differing atmospheric and land components, ACCESS1.0 and ACCESS1.3. The former includes the Met Office (UKMO) atmospheric and land components found in the HadGEM2 model (Collins et al. 2008). The UKMO atmospheric model has a zonal resolution of 1.875° and 1.25° in the meridional direction with 38 vertical levels and uses the Smith (1990) cloud scheme; the atmosphere and ocean are coupled to the Met Office Surface Exchange Scheme (MOSES) land surface scheme (Essery et al. 2001). In contrast, ACCESS1.3 uses an interim developmental atmospheric component of Hadley Centre Global Environment Model, version 3 (HadGEM3; Hewitt et al. 2011), with the Australian CSIRO Atmosphere Biosphere Land Exchange (CABLE) land surface scheme and the prognostic cloud fraction and prognostic condensate scheme (PC2; Wilson et al. 2008). The atmospheric resolution is the same as for ACCESS1.0.

In contrast, ESM2M and ESM2G (Dunne et al. 2012) include the same land, ice, and atmosphere components but different ocean models. ESM2M uses a depth-coordinate model with 50 vertical layers, whereas ESM2G uses an isopycnal-coordinate model with 59 density layers beneath the two bulk mixed layers and two buffer layers. The ocean interior variables analyzed here for ESM2G have been interpolated onto the ESM2M depth grid. In section 4, we discuss the ramifications of having four models used in the eddy compensation part of this study with the MOM4p1(Griffies 2007) ocean model (i.e., ACCESS1.0, ACCESS1.3, ESM2M, and CM3).

The climate response of the 13 models is assessed using two CMIP5 experiments, namely the historical (HIST) and the representative concentration pathway (RCP8.5), reaching a radiative forcing of 8.5 $\mathrm{W\,m^{-2}}$ by 2100 (Moss et al. 2010; Taylor et al. 2012). The historical experiment is based on observed natural and anthropogenic atmospheric changes and is run between 1850 and 2005. The RCP8.5 is the highest emission scenario in the CMIP5 experiments and, in comparison to the equivalent global atmospheric CO_2 concentration reached by 2100, it significantly exceeds the high Special Report on Emission Scenarios (SRES) A2 in the CMIP3 effort by several hundred parts per million (Moss et al. 2010). We compare two 20-yr periods [HIST (1986–2005) and RCP8.5 (2081–2100)] and have chosen the first model ensemble (r1i1p1) for all models, as in most cases this is all that is available. We only have four models for the analysis of the sensitivity of the MOC in density space to winds and buoyancy fluxes (section 3c) and so to provide a more statistically robust experiment we also use 5-yr means across the 150-yr period of 1950–2100 spanning parts of the HIST and RCP8.5 experiments. Our results are not free of model drift (we discuss this further in section 4), which has been suggested to influence the ocean density (e.g., Sloyan and Kamenkovich 2007) but is less likely to greatly change the main ACC transport and MOC conclusions (e.g., Sen Gupta et al. 2009; Wang et al. 2011; Voldoire et al. 2013).

b. Observationally based estimates

Throughout this study, we compare the model estimates with those derived from observations. For heat, freshwater, and momentum fluxes we use the Common Ocean–Ice Reference Experiment, version 2 (CORE.v2), global air–sea flux dataset. Detailed descriptions of the methods and data included can be found in Large and Yeager (2009). This dataset has been obtained from the Research Data Archive (RDA; http://rda.ucar.edu; dataset number ds260.2), which is maintained by the Computational and Information Systems Laboratory (CISL) at NCAR, sponsored by the National Science Foundation (NSF). The CORE.v2 dataset uses the National Centers for Environmental Prediction (NCEP) atmospheric state, and the NCEP wind speeds have been corrected using Quick Scatterometer (QuikSCAT) satellite observations. Radiative fluxes are derived from satellite measurements, and the temperatures for the radiative flux calculations are from the Hadley Centre Sea Ice and Sea Surface Temperature dataset (HadISST) temperature–ice climatology. Precipitation in the Southern Ocean (65°–30°S) is from the Climate Prediction Center Merged Analysis of Precipitation (CMAP) product. The interior ocean density is based on the temperature and salinity data in the CSIRO Atlas of Regional Seas released in 2009 (CARS2009; Ridgway et al. 2002). We use monthly-mean output averaged over the 1986–2005 period. Several estimates of the ACC transport using hydrographic data and assimilated solutions have been documented since the 1980s and many of these are given by Griesel et al. (2012, their Table 1). Estimates range from 134 to 164 Sv ($1\,\mathrm{Sv} = 10^6\,\mathrm{m}^3\,\mathrm{s}^{-1}$), including the commonly cited 136.7 ±7.8 Sv estimated by Cunningham et al. (2003) using cruise data.

3. Results

a. The Antarctic Circumpolar Current transport

Here, we quantify the ACC transport in the HIST (1986–2005) and RCP8.5 (2081–2100) periods in the CMIP5 ensemble and its relationship with surface momentum, heat, and freshwater fluxes. We begin with wind stress forcing (Fig. 1). In the HIST period, the modeled wind stress varies between 0.16 and 0.25 Pa, slightly higher than the observed 0.15 Pa. The wind forcing in 12 models increases by 0.005 to 0.045 Pa at the end of the twenty-first century, in agreement with Swart and Fyfe (2012, comparing our Fig. 1 with their Fig. 4). The models' Drake Passage ACC transports in the HIST period range between 78 and 253 Sv. Five of the models (models 1, 5, 7, 9, and 11) fall within the observed ACC transport range of 134–164 Sv given in Table 1 of Griesel et al. (2012). Under RCP8.5 forcing, the ACC transport changes by $\sim\pm15\%$. We find increases in half of the models (1, 3, 4, 7, 9, and 13) and decreases in the rest. In the mean and projected state, we find no significant correlation between the maximum strength of the zonal wind stress between 65° and 45°S and the ACC transport. This weak sensitivity is opposite to expectations from coarse-resolution ocean-only simulations but is in agreement with previous studies analyzing the CMIP3 models (e.g., Sen Gupta et al. 2009). The latitude of the wind stress maximum is also unrelated to the strength of the ACC transport in the mean and projected states.

The dependence of ACC transport upon heat and freshwater fluxes is shown in Fig. 2. The surface heat flux is a combination of the sensible, latent, longwave radiation, and shortwave penetrative radiation. The freshwater flux (FW) is the sum of the precipitation into the ocean (including that from snow and sea ice melt), evaporation of freshwater from the ocean, and river runoff. We average the heat and freshwater fluxes over the regions north and south of the wind stress maximum (see Fig. 1). As expected, in the HIST and RCP8.5 periods, the heat gain is larger north of the wind stress maximum than the south and vice versa for the freshwater input. The models are in better agreement with observations and with the other models for the buoyancy fluxes averaged north of the wind stress maximum, compared with the southern averages. The models show a consistently strong correlation between the north and south freshwater inputs and the ACC transport. We find that models with a larger freshwater difference across the ACC region are associated with a stronger zonal flow, noting that the sign of this difference is opposite to what would fulfill the thermal wind relation.

Over the twenty-first century, increases in the heat and freshwater input south of the wind stress maximum (up to $14\,\mathrm{W\,m}^{-2}$ and $0.9 \times 10^{-5}\,\mathrm{kg\,m}^{-2}\,\mathrm{s}^{-1}$, respectively) are larger than the northern changes (up to $5\,\mathrm{W\,m}^{-2}$ and $0.4 \times 10^{-5}\,\mathrm{kg\,m}^{-2}\,\mathrm{s}^{-1}$, respectively; Fig. 3, top versus middle panels). The heat loss south of the wind stress maximum becomes an overall heat *gain* (Fig. 2, red points in top panel). This causes the south-minus-north difference in heat flux (which was negative in the HIST period) to be reduced (Fig. 3, bottom panel). Increased heat gain in the southern region and increased freshwater input in the northern region are associated with

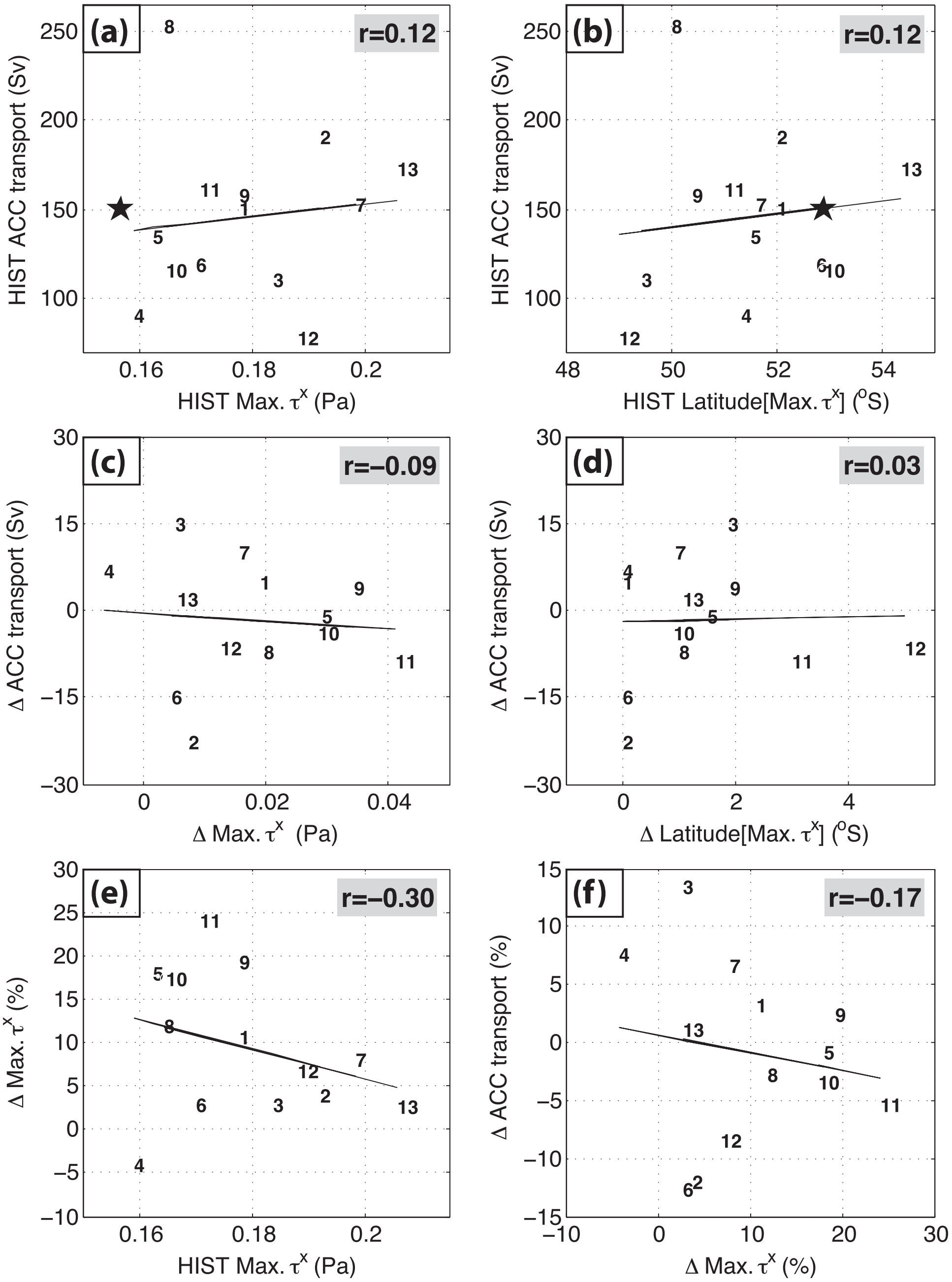

FIG. 1. (a) The maximum zonally averaged zonal-wind stress between 60° and 45°S ($\tau^x_{\max}$; Pa) vs the ACC transport (Sv) for the HIST period. (b) The latitude of this maximum zonal-wind stress (lat[max τ^x]; °S) for the HIST period. (c),(d) As in (a),(b), but for the RCP8.5 − HIST difference (Δ). (e) The maximum zonal-wind stress for the HIST period (Pa) vs its change as a percentage. (f) The percentage changes in the zonal-maximum wind stress and the ACC transport. The black stars are observationally based estimates of the zonal-wind stress and latitudes from the CORE.v2 climatology. The numbers correspond to models in Table 1; the solid black lines are the lines of best fit for the 13 model points, and the correlation coefficients (none of which are significant at the 90% level) are shown in the gray boxes.

a larger ACC transport decrease. Similarly, a larger weakening of the heat flux south-minus-north difference (i.e., higher positive red values in the bottom of Fig. 3) is associated with a decrease in ACC transport.

A shift in the position of the westerlies can alter the spatial position of upwelling and downwelling regions, high precipitation bands, and the heat fluxes driven equatorward in the Ekman layer. Figure 4 shows that

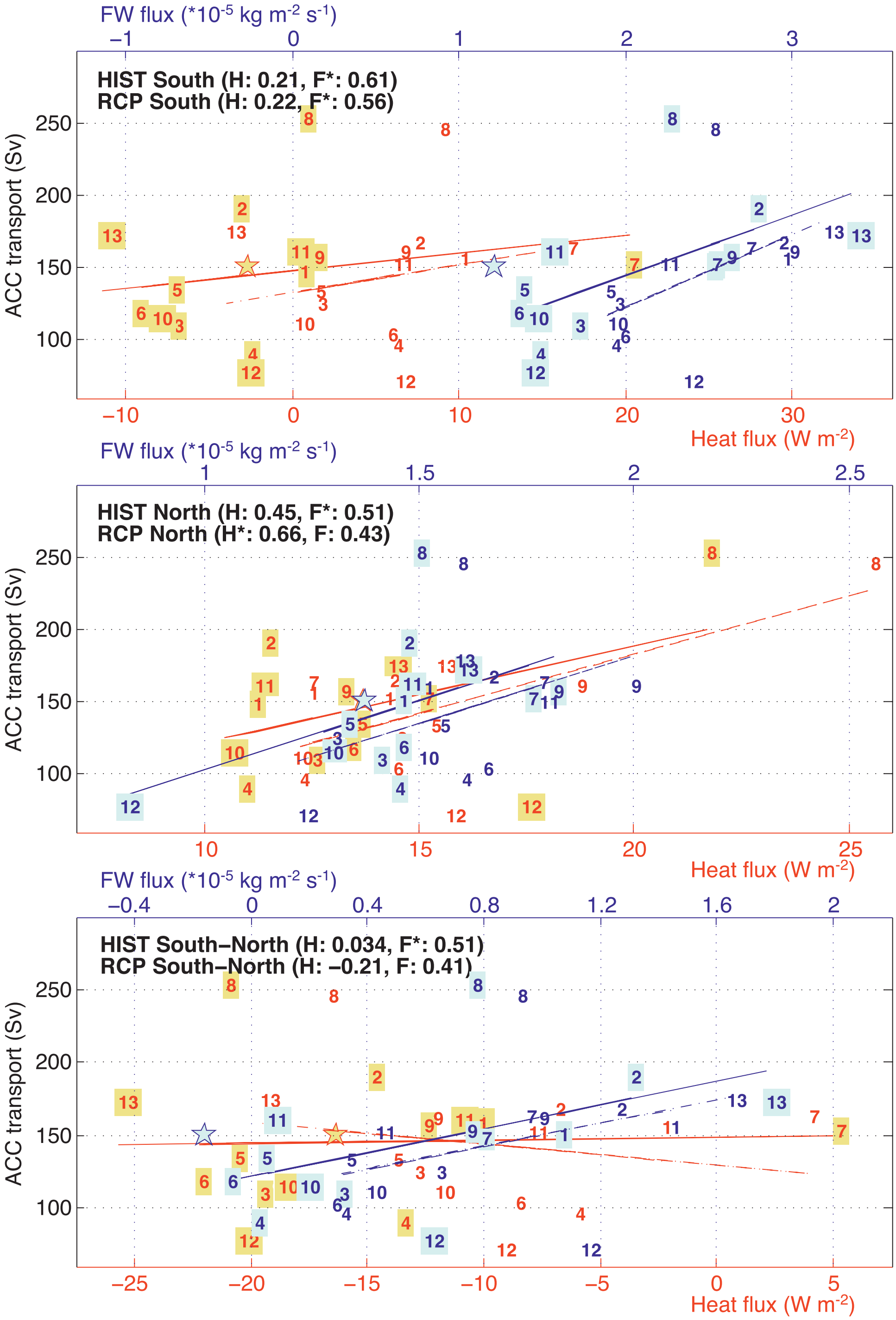

FIG. 2. Surface heat (red; W m^{-2}) and FW (blue; 10^{-5} kg m^{-2} s^{-1}) fluxes for the 13 numbered models (numbers) and observations (stars) vs ACC transport (*y* axis; Sv). Note that the yellow star (representing the observed heat flux) in the middle panel is directly underneath the blue star. Both the heat and FW fluxes are positive into the ocean. HIST values are shaded yellow (heat) and blue (FW) whereas RCP8.5 values are unshaded. The line of best fit is shown by the solid line for the HIST period and the dashed line for the RCP8.5 period. (top) Buoyancy fluxes averaged between 65°S and the latitudes of the wind stress maximum (Fig. 1). (middle) Buoyancy fluxes averaged between the wind stress maximum and 45°S. (bottom) The difference between the fluxes in (top) and (middle) (i.e., buoyancy fluxes across 65°–45°S). The correlations between ACC transport and the heat (*H*) and freshwater (*F*) fluxes are given in the parentheses in the panel titles; the asterisks indicate significant correlations at the 90% level.

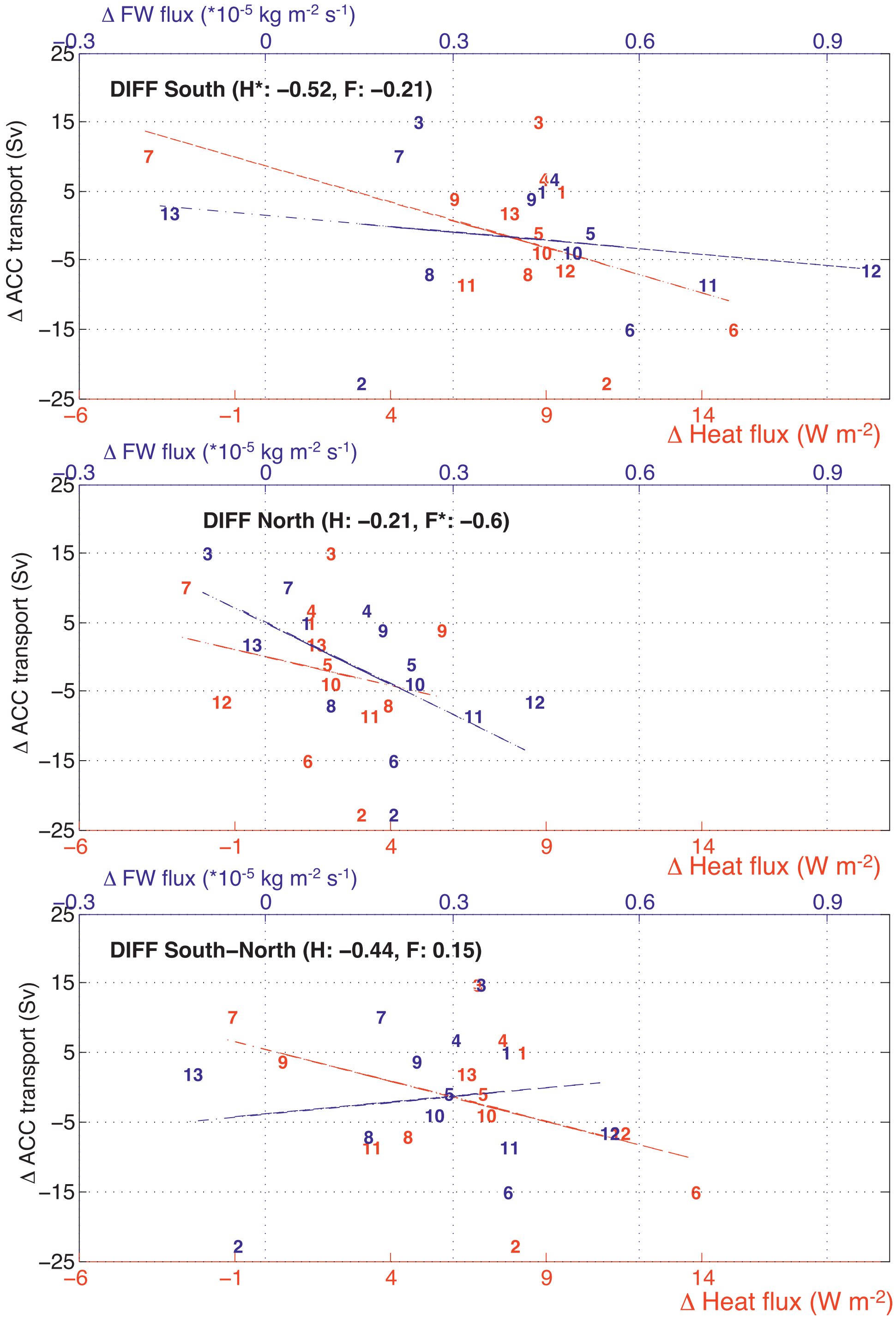

FIG. 3. As in Fig. 2, but only for the 13 numbered models for the RCP8.5 − HIST difference. The line of best fit is shown by the dashed line.

increased freshwater input north and south of the wind stress maximum are strongly associated with a poleward increase in the latitude of that maximum. The correlation coefficients are significant at the 90% level (but not the 95% level). The freshwater increase south of the wind stress maximum is stronger than that to the north and provides more freshwater to be carried northward in the Ekman layer when the westerlies shift poleward.

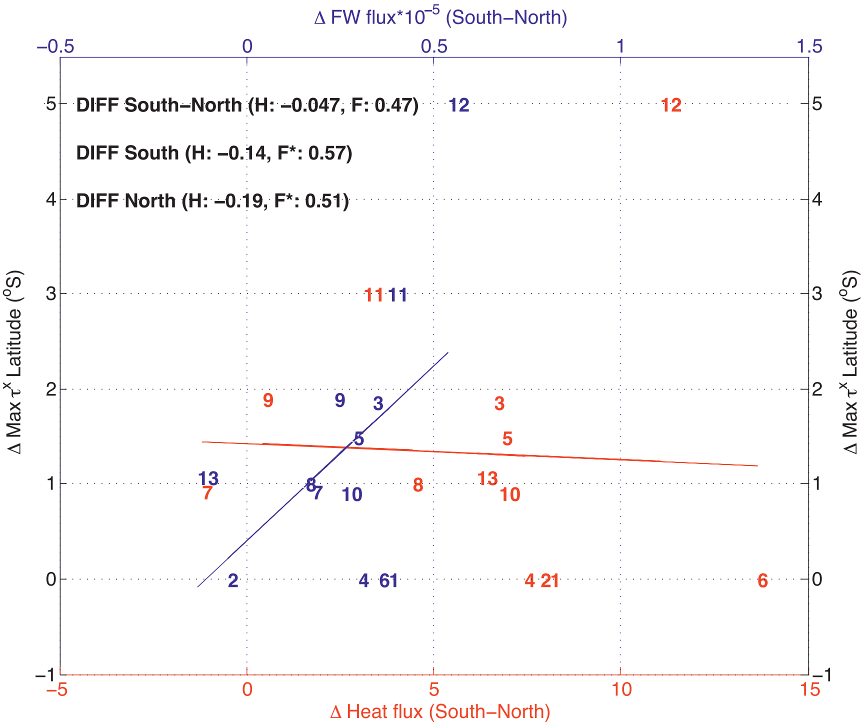

FIG. 4. Surface heat (red; W m^{-2}) and FW (blue; 10^{-5} kg m^{-2} s^{-1}) fluxes for the 13 numbered models vs the latitude of the wind stress maximum (see Fig. 1) for the RCP8.5 − HIST period. We have only illustrated the buoyancy fluxes across 65°–45°S (i.e., south − north fluxes). However, we also have listed the correlation coefficients for the north and south averaged buoyancy fluxes; the asterisks indicate significant correlations at the 90% level. The line of best fit for the models is shown by the red and blue lines on each panel.

Conversely, changes in the heat flux are unrelated to changes in the position of the westerlies.

In their analysis of 19 CMIP3 models, Wang et al. (2011) showed that increased wind-driven downwelling in the northern part of the ACC region competed with the increased southern buoyancy changes and that a poleward wind shift resulted in a greater area for downwelling. Here, the ACC transport changes under RCP8.5 forcing are not directly related to changes in the wind stress strength or position but rather to the difference in heat and freshwater differences in the upwelling and downwelling regions, indicating that buoyancy fluxes play a dominant role in ACC transport trends. We do note, however, that a poleward shift in the westerlies may indirectly influence the ACC transport changes via surface freshening.

We analyzed the zonally averaged Southern Ocean density in the 13 models for the HIST (1986–2005) period, compared with observationally based estimates (CARS2009) in Fig. 5. We find the models are all lighter than observed in the upper 2000 m, with a nonuniform agreement between observation–model differences below this depth. The CSIRO Mk3.6, CanESM2, FGOALS, and NCAR-CCSM4 models, in particular, are denser than observed and their density surfaces lighter than $\sigma_0 < 1027.8$ kg m^{-3} are concentrated in the upper 2 km. In the RCP8.5 experiment (see red contours in Fig. 5), all the models lighten via ocean warming and freshening in the upper 2000 m and stratification increases (Fig. 6). The isopycnal slopes change in some models (e.g., ACCESS1.3 south of 60°S in Fig. 5); however, the slope gradient changes are minimal in comparison to studies where the winds are increased by a factor of at least 2 (e.g., Farneti et al. 2010).

We find that the 13 CMIP5 models studied here exhibit smaller changes in their ACC transport (~±15%) relative to the changes in the overlying wind stress (~0%–25%; see Fig. 1f). Overall the increased ocean surface buoyancy gain overwhelms the moderate wind stress changes and appears to be the primary driver of ACC transport changes under RCP8.5 forcing. We find that a poleward shift in the wind stress maximum correlates with an intensification of the hydrological cycle but not with ACC transport changes. Testing the relationship between winds and freshwater fluxes in a

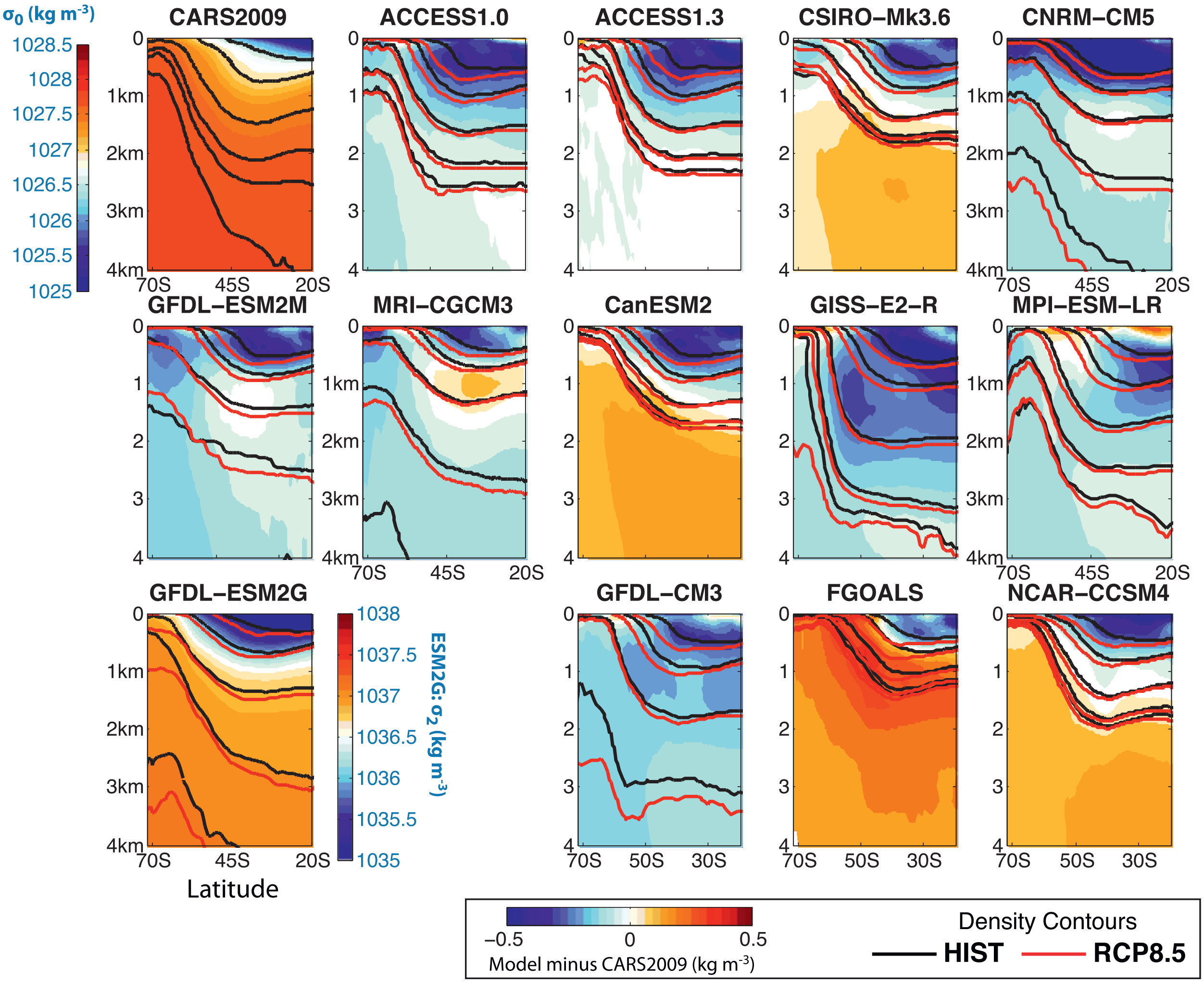

FIG. 5. Density for the HIST (colors and black contours) and RCP8.5 (red contours) experiments. (top left) The CARS2009 climatology with six density surfaces highlighted (kg m^{-3}): 1026.5, 1027, 1027.5, 1027.7, 1027.75, and 1027.8. The same six surfaces and the difference between the models and CARS2009 are shown in the subsequent nine panels. In the ESM2G model, the density field is outputted on the model's σ_2 coordinate and the difference from observations is thus not shown. The other 12 models show σ_0. The ESM2G HIST and RCP8.5 σ_2 contours are (kg m^{-3}) 1035, 1036, 1036.8, 1037, and 1037.1.

coupled framework is complicated by atmosphere–ocean feedbacks and would require additional model sensitivity experiments.

b. Compensation of the meridional overturning cells

We now shift our focus to the modeled MOC, for the HIST and RCP8.5 periods, in relation to the overlying surface wind and buoyancy fluxes. We are first interested in how the meridional overturning circulation varies under climate change forcing and begin with a comparison of MOC between the HIST and RCP8.5 20-yr periods in depth (Fig. 7) and density (Fig. 8) space. The MOC is the sum of the Eulerian time-mean ($\overline{\Psi}$) and eddy-induced (Ψ^*) overturning. The former is given by the streamfunction, defined by the zonally integrated Eulerian-mean meridional velocity ($\overline{v}$) over the vertical height of the grid cell (Griffies 2012) $\overline{\Psi}(y,z,t) = -\int dx \int \overline{v}\rho\, dz$, whereas the eddy overturning is based on the constant density (ρ_0), the zonally integrated model eddy diffusivity (κ), and the isopycnal slope ($\mathbf{S} = -\nabla_h\rho/\partial_z\rho$; Griffies 1998) $\Psi^*(y,z,t) = \rho_0 \int dx(\kappa\mathbf{S})$. The overturning streamfunctions are calculated in units of kilograms per second and divided by ~1000 kg m^{-3} to give units of Sverdrups. The overturning circulation is estimated explicitly at each model time step in depth space. Models 1, 2, 5, and 7 also integrate the streamfunctions to density space. The residual MOC is estimated by adding the three-dimensional (i.e., zonally summed and time varying) Eulerian and eddy MOC fields and then taking the maximum cell strength in the "upper" and "lower" box regions defined below.

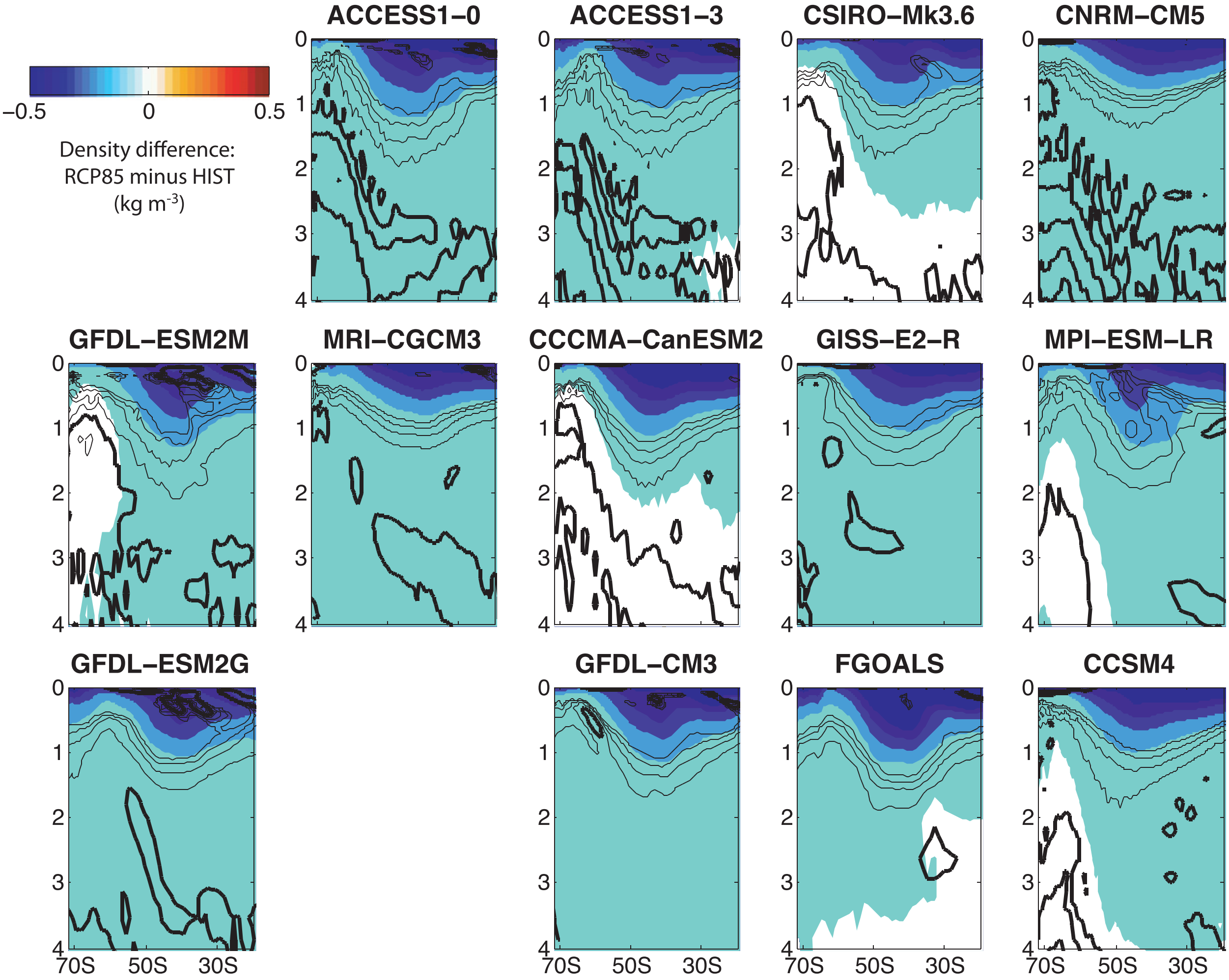

FIG. 6. Density for the RCP8.5 − HIST (colors; kg m^{-3}) with the difference in the potential vorticity overlaid (0 contour thick solid; thin solid indicates increased potential vorticity, that is increased stratification in contour intervals of 5×10^{-12} m^{-1} s^{-1}). Potential vorticity is calculated as $-(f/\rho)(\partial\rho/\partial z)$, where ρ is the mean density and z is the vertical coordinate. This approximation effectively assumes that the relative vorticity is negligible for large-scale flows. A higher potential vorticity implies increased stratification (and weaker mixing).

We separate the depth–space overturning circulation in eight models into upper (magenta box bounded by 65°–40°S and depth of 0–3500 m) and lower (magenta box bounded by 50°–30°S and depth of 2500–5000 m) cells, each composed of an Eulerian and eddy contribution (Fig. 7). The Eulerian upper cell is a clockwise circulation composed of the wind-driven northward transport of upwelled southward-flowing deep waters in the shallow Ekman layer that are then subducted into the ocean interior as mode and intermediate waters (cf. Speer et al. 2000). The models' Eulerian upper cell maximum strength ranges between 28 and 45 Sv across the eight models (Fig. 7; red values in Fig. 9a). The Eulerian lower cell is a counterclockwise flow of denser upwelled southward-flowing deep waters that then sink to the abyssal ocean and are exported equatorward as Antarctic Bottom Water. This cell ranges between −3 and −18 Sv in the models; negative values indicating anticlockwise circulation (Fig. 7; red values in Fig. 9d). The eddy overturning cell (middle, Fig. 7) flows in the counterclockwise direction, enhancing the lower cell circulation and weakening the upper cell. The eddy MOC cells average at about 15 (eddy upper) and 10 Sv (eddy lower). We find the Eulerian and eddy MOC cell strengths across the eight models agree favorably with previous inverse model-based estimates (e.g., Lumpkin and Speer 2007; Sloyan and Rintoul 2001) despite differing substantially in the spatial position and area of the cells.

Only half of the eight models also archive MOC in density space, and we describe the circulation briefly here. We note only having output for four models does

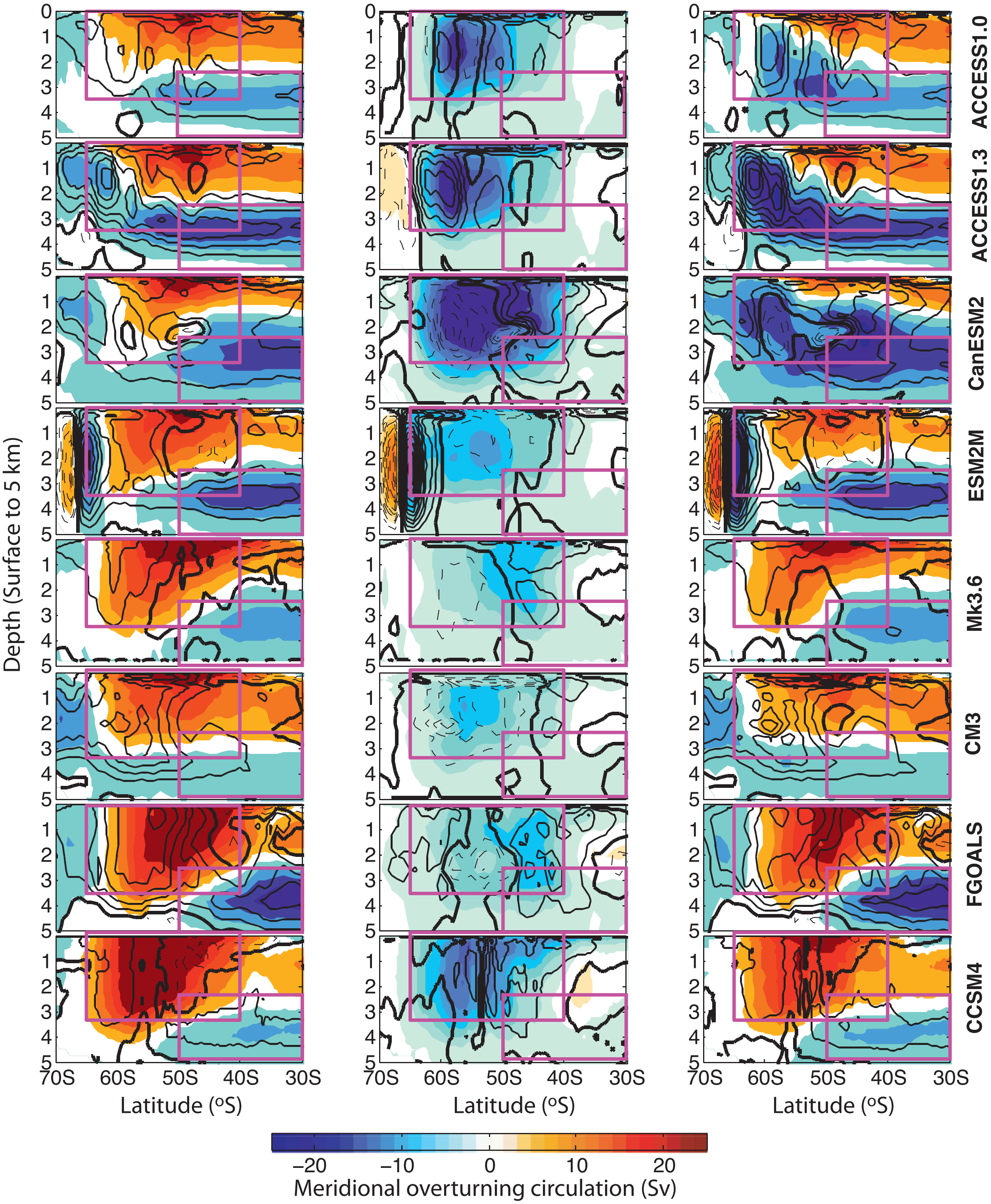

FIG. 7. The (left) Eulerian, (center) eddy, and (right) residual maximum strength of the MOC cells in depth space for eight CMIP5 models. Colors represent the HIST 1986–2005 average. Contours represent the positive (solid), zero (bold solid), and negative (dashed) change in the MOC (i.e., RCP8.5 − HIST). Contour intervals for (left) and (right) are 3 Sv and 1 Sv for (center). The *y* axis is depth (km) with latitude on the *x* axis. The magenta boxes encapsulate the upper (65°–40°S; depth of 0–3500 m) and lower (50°–30°S; depth of 2500–5000 m) cell regions used for estimating the maximum cell strengths in Figs. 9 and 10.

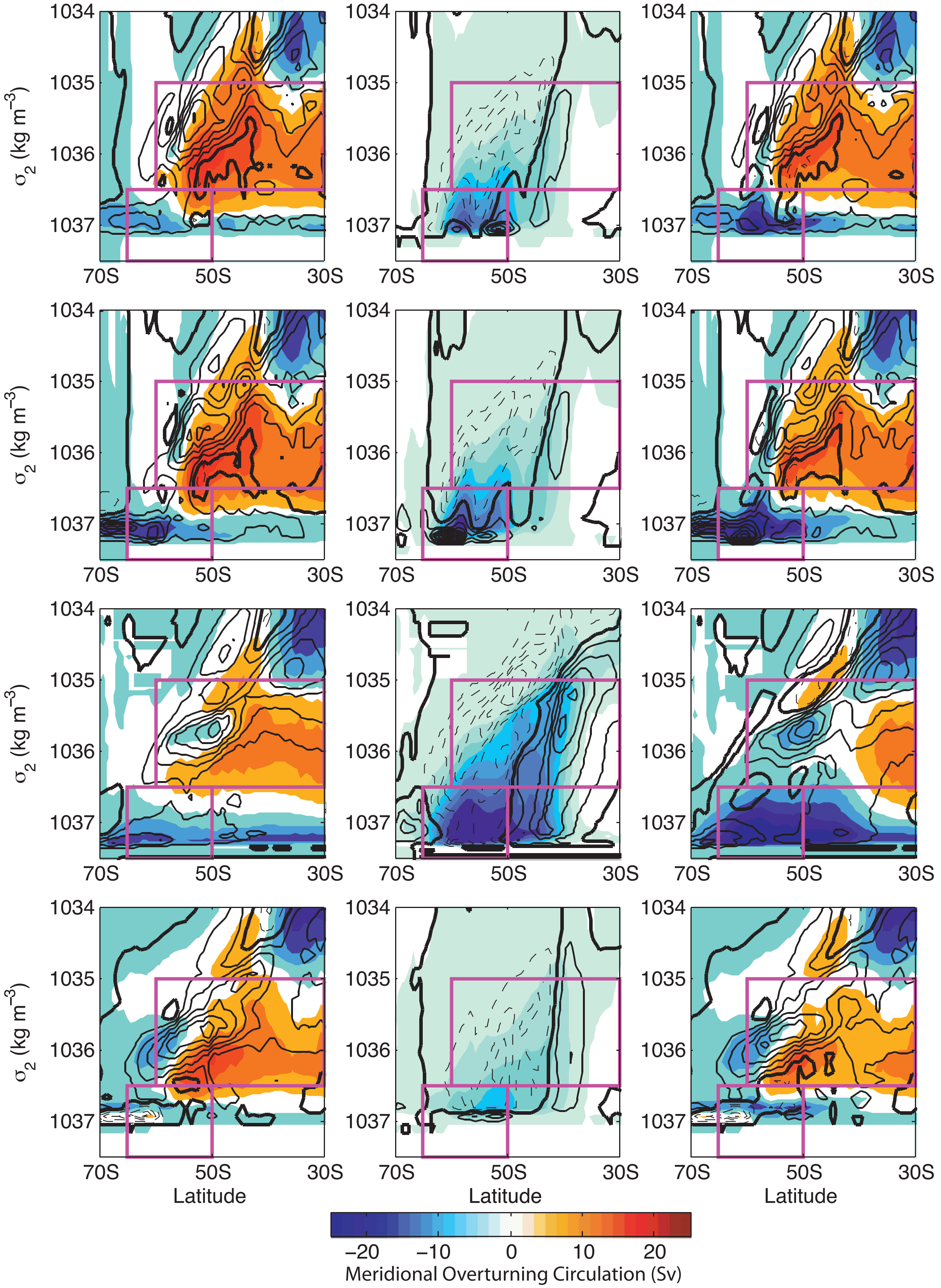

FIG. 8. As in Fig. 7, but for the residual MOC in density space for (top)–(bottom) the ACCESS1.0, ACCESS1.3, CanESM2, and ESM2M models. The *y* axis here is density (σ_2; kg m^{-3}). The magenta boxes encapsulate the upper (60°–30°S; σ_2 of 1035–1036.5) and lower (65°–50°S; $\sigma_2 > 1036.5$) cell regions.

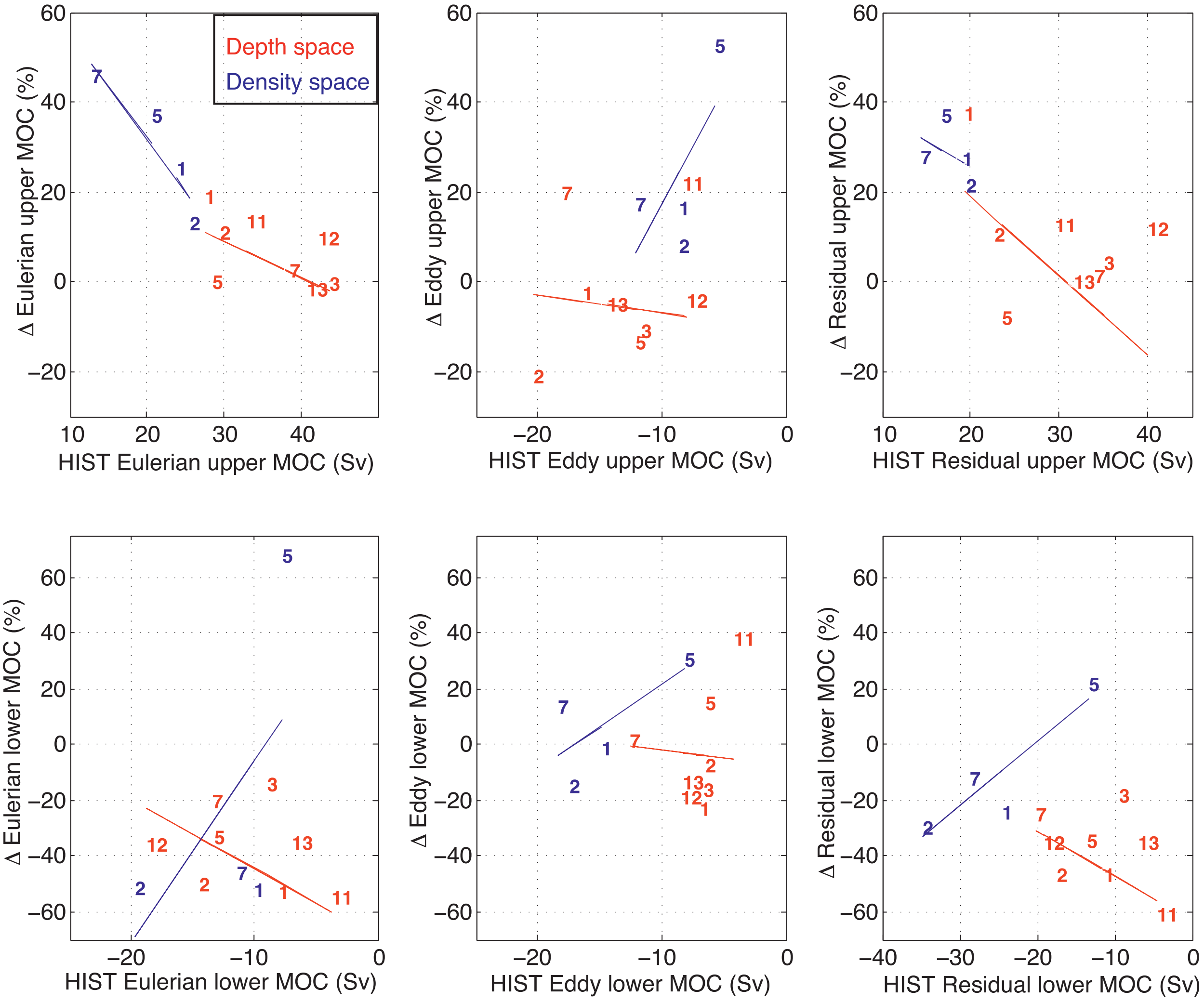

FIG. 9. The (left) Eulerian, (center) eddy, and (right) residual MOC in depth (red; eight models) and density (blue; four models) space as an overturning rate (Sv) or as a percentage of change relative to the HIST period (Δ%; positive indicates increase). (top) Upper overturning and (bottom) lower overturning. The lines of best fit for the four models with MOC are in depth and density spaces only (i.e., models 1, 2, 5, and 7). For the HIST overturning strength (Sv; *x* axis), positive indicates a clockwise overturning cell and negative indicates an anticlockwise cell. For the change in overturning (*y* axis), positive indicates an increase and negative a decrease.

place a considerable restriction on our MOC analysis in density space; however, water masses associated with MOC flow most easily along density surfaces (cf. Hallberg and Gnanadesikan 2006), and it is clear that the density–space MOC is more physically realistic. We separate the density–space overturning circulation into the upper cell (magenta box bounded by 60°–30°S; σ_2 is 1035–1036.5) and lower cell (magenta box bound by 65°–50°S; $\sigma_2 > 1036.5$). The Eulerian upper and lower cells flow in the same direction as in depth space (Fig. 8; blue values in Fig. 9). In the HIST period, the Eulerian upper cell ranges in strength from 13 to 26 Sv and from −8 to −20 Sv for the Eulerian lower cell. The key difference between the depth and density frameworks is that in density space the eddy overturning cell is strongest in the lower cell region (from −8 to −18 Sv in density space versus from −4 to −12 Sv in depth space), and in three of the four models the eddy lower cell is stronger than the Eulerian lower cell. The inverse model used by Lumpkin and Speer (2007) shows density–space residual upper and lower cell strength of 15 Sv; however, they do not explicitly resolve eddy fluxes. The four CMIP5 models analyzed here show a similar maximum strength of the residual upper cell (albeit located farther poleward) and a stronger residual lower MOC cell.

By the end of the twenty-first century, the Eulerian upper cell in depth space strengthens by up to 20% (up to 5 Sv) and the Eulerian lower cell weakens by 10%–60% (1–7 Sv; Figs. 7, 9). Most of the eight models project weakened eddy upper and lower cells by up to 20% (up to 4 Sv); the exceptions are models 7 and 11 (CanESM2 and GFDL-CM3) that show strengthened eddy overturning cells by 20%–40%. In the density space under RCP8.5 forcing, we find the models project a strengthening of the upper Eulerian and eddy cells by 20%–40%, similar to the changes projected in depth space; however, the HIST cell strengths are smaller than in depth space (Figs. 8, 9). Three of the four models (ESM2M being the exception) project a weaker Eulerian lower cell; ACCESS1.3 projects the largest decrease in the residual lower overturning (10.3 Sv) based on large changes in the lower Eulerian cell and a large decrease in ACC transport. In both depth and density spaces, the models vary in the size, strength, and spatial location of their MOC cells, leading to large differences in the HIST and RCP8.5 periods (Fig. 9). We found that the projected changes in Eulerian and eddy cell strength, and those changes relative to the HIST period, varied over a wider range in density space than in depth space. In particular, ESM2M (model 5) showed a larger increase in the strengthening of the eddy cells in density space and a different sign in the change in the Eulerian lower cell.

Eddy compensation here is where the changes in the Eulerian upper (lower) cell are balanced by opposing changes in the eddy upper (lower) cell. In Fig. 10, we plot the change in the residual overturning (Figs. 10a,b), which takes into account the difference in the spatial positions of the Eulerian and eddy cells and the changes separated into the Eulerian and eddy components (Figs. 10c,f). For the upper and lower cells in both depth and density spaces, we find that the models show partial eddy compensation at best, in agreement with high-resolution studies (e.g., Hallberg and Gnanadesikan 2006; Farneti et al. 2010; Meredith et al. 2012). Models 3, 5, and 13 show signs of eddy compensation for the upper cell in depth space; however, this is primarily due to minor changes in the strength of these cells under RCP8.5 forcing (Figs. 10c,d). Overall, we find the models exhibit partial eddy compensation under RCP8.5 forcing. We have discussed the MOC results in both depth and density spaces in this section, but in the final results section we focus on trends solely in density space, given that water mass circulation flows naturally in this framework.

c. The influence of surface fluxes on overturning in density space

Obviously we cannot acquire a statistically significant multimodel conclusion of the influence of surface fluxes in varying the MOC in density space by assessing two 20-yr averages in only four models. Thus, we use 5-yr averages of monthly calculations over the 1950–2100 (HIST and RCP8.5 combined) period and assess the evolution of MOC trends with respect to wind- and buoyancy-based variables. Figure 11 illustrates the relationships between MOC cells and wind and buoyancy fluxes, separated into southern upwelling and northern downwelling regions, and Table 2 summarizes the significant correlations. Ekman suction and pumping, the upwelling and downwelling transport driven by winds, are defined as $\mathbf{W}_{\mathrm{Ek}} = \mathbf{\nabla} \times \boldsymbol{\tau}/\rho f$, where the surface zonal and meridional wind stress is given by $\boldsymbol{\tau} = (\tau^x, \tau^y)$, ρ is the surface density, and f is the Coriolis parameter. We integrate the Ekman pumping over the ocean surface area to give units in Sverdrups. Ekman pumping is positive upward. The northward Ekman transport resulting from the eastward-flowing Southern Hemisphere zonal winds $V_{\mathrm{Ek}} = -\tau^x/\rho f$ is integrated meridionally to give units in Sverdrups.

The correlations between the wind-based variables and the strength of the Eulerian and eddy upper cells and lower Eulerian cell over the 150-yr period are uniform and significant across all four models. Wind stress, Ekman pumping and suction, and northward Ekman transport overlying the lower and upper cell latitudes are projected to increase the clockwise (MOC) circulation associated with the strengthening of the upper Eulerian cell and weakening of the lower Eulerian cell. The sign of the evolution of the lower eddy MOC cell differs between the ACCESS models and CanESM2 and ESM2M, possibly related to the minimal shift in the westerlies in the ACCESS models versus a significant poleward shift in the other two models (see Fig. 1).

We found that increased surface heat gain to the ocean is correlated with the evolution of the MOC cells over the 150-yr period. There is a clear correspondence between the heating of the upper cell and the increases in the Eulerian MOC, with partial compensation by increases in the eddy MOC. The correlations between increases in surface freshening and the MOC cells are weak and nonuniform in strength and sign across the four models. The deep waters that upwell in the Southern Ocean may have a stronger correlation with their northern formation–outcrop regions. We find that the latitudes of the Eulerian and eddy cell maximum shift poleward in response to a lightening of the density associated with this maximum, most notably for the upper Eulerian cell (not shown). We note that most of the MOC cells remained at a similar density over the 150-yr period, associated with weak density changes in the abyssal ocean. Also, the latitude of the wind stress maximum fluctuates over the 150-yr period, thus making it difficult to draw strong conclusions about its role in influencing the strength of the MOC cells in density space. We find the

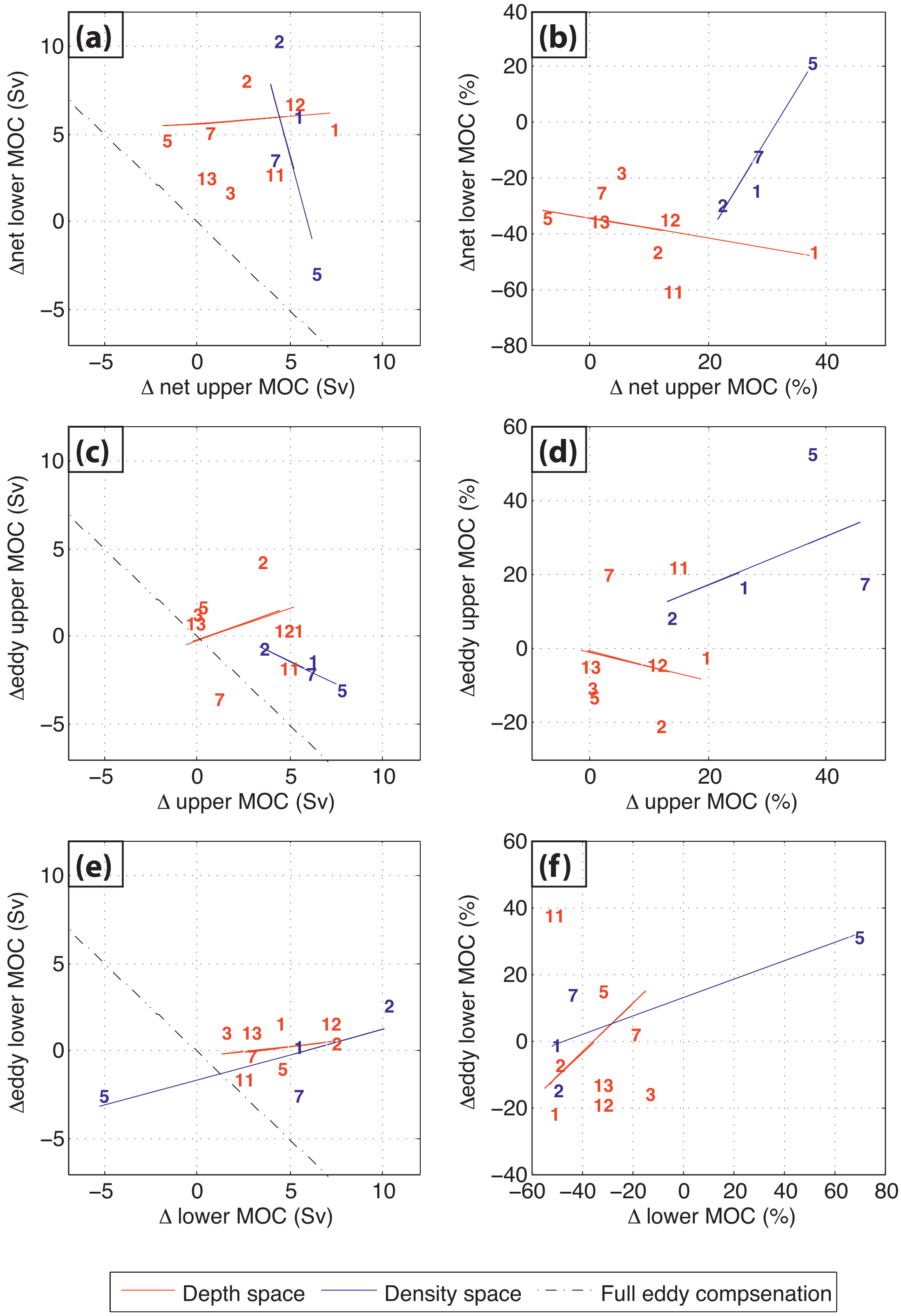

FIG. 10. Change relationships between overturning cells for the RCP8.5 − HIST period in depth (red; eight models) and density (blue; four models) space: change in (left) Sverdrups and (right) percent relative to the HIST period (i.e., positive implies and increase). (a),(b) The change in the residual upper cell vs residual lower cell. (c),(d) The change in the Eulerian vs eddy upper cells. (e),(f) The change in the Eulerian vs eddy lower cells. A black dashed line indicating eddy compensation (i.e., the change in the Eulerian cell is balanced exactly by the change in the eddy cell) is overlaid in (a),(c). Red and blue lines of best fit for the four models with MOC are in depth and density spaces only (i.e., models 1, 2, 5, and 7).

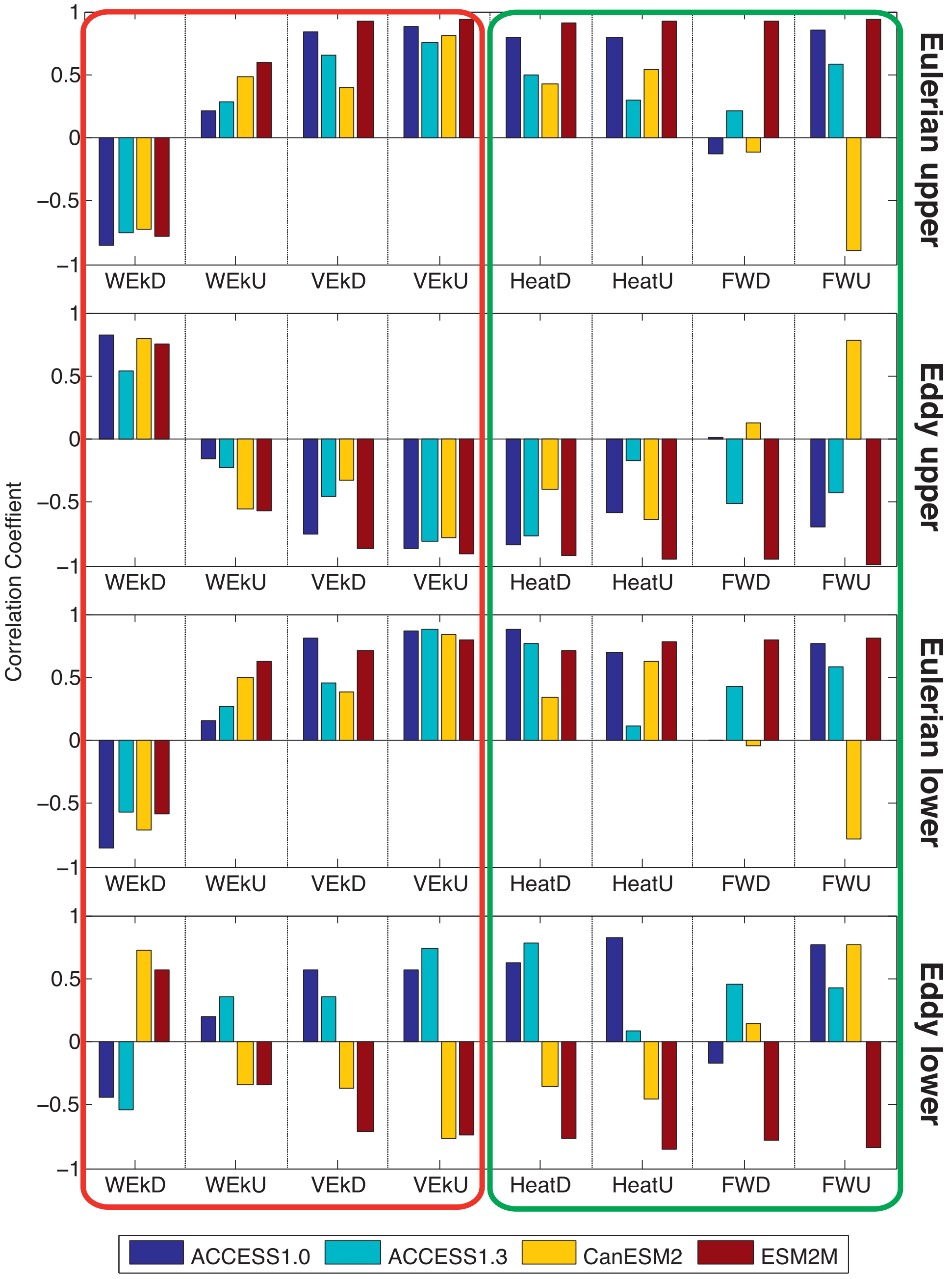

FIG. 11. Correlation between the 1950–2100 5-yr averages in the maximum strength of the Eulerian and eddy upper and lower MOC cells and (left) wind and (right) buoyancy-based variables for ACCESS1.0 (dark blue), ACCESS1.3 (light blue), CanESM2 (yellow), and ESM2M (red). Shown are the correlations between changes in the MOC and those found from left to right in Ekman pumping (WEkD) and Ekman suction (WEkU) and northward Ekman transport (VEkD, VEkU), HeatD, HeatU, FWD, and FWU—the heat and freshwater fluxes in the downwelling and upwelling regions, respectively. The downwelling region is associated with the north side of the wind stress maximum and upwelling with the south. See text for a description of the formulas for all variables and Table 2 for the interpretation of the correlation coefficients.

four CMIP5 models analyzed are significantly influenced by the strength of the overlying westerlies; however, the relationship between MOC changes and buoyancy fluxes (particularly freshwater fluxes) remains unclear.

4. Summary and discussion

We quantify the response of the ACC transport and MOC under the RCP8.5 climate forcing, in association

TABLE 2. Summary of patterns for surface-based buoyancy and momentum fluxes over 1950–2100 (HIST and RCP8.5 experiments combined) associated with changes in the MOC cells strengths in density space (see Fig. 11). The term $\tau^x_{\max}$ is the maximum zonal-mean wind stress and HeatD and HeatU/FWU are the heat and freshwater fluxes in the northern downwelling and southern upwelling regions, respectively. The patterns described are those found for at least three of the four models; see text for exceptions. The heat and freshwater fluxes in the upwelling region (HeatU and FWU) did not show uniform significant correlations or signs of the correlation with overturning cell patterns.

MOCρ cell	150-yr trend in MOCρ	Wind–buoyancy trend significantly correlated with MOCρ trend
Eulerian upper	Increased clockwise overturning	$\tau^x_{\max}$ strengthened; HeatD and HeatU: warmer
Eddy upper	Increased anticlockwise overturning	$\tau^x_{\max}$ strengthened; HeatD and HeatU: warmer; FWU: fresher
Eulerian lower	Decreased anticlockwise overturning	$\tau^x_{\max}$ strengthened; HeatD and HeatU: warmer; FWU: fresher
Eddy lower	Decreased (models 1 and 2)/increased (models 5 and 7)	$\tau^x_{\max}$ strengthened; HeatD and HeatU: warmer

with changes in the overlying surface wind, heat, and freshwater input, in 13 CMIP5 coarse-resolution coupled climate models. Our main results are summarized in Fig. 12. In the HIST period (1986–2005), models with greater freshwater flux are associated with a stronger ACC transport. The freshwater flux south-minus-north difference across the ACC region is of a sign that should act to *decrease* the thermal wind forcing of the ACC, implying either that it is the total freshwater flux that is controlling the ACC or that higher-order dynamics than thermal wind are operating here. Under RCP8.5 forcing, the ACC transport changes minimally or decreases in models that project a larger reduction in the south-minus-north difference in the heat flux (due to increased heat gain to the south) and increased freshwater input in the northern ACC region. The additional heat flux appears to be a direct result of the warming surface air temperature, while the freshwater fluxes increase through precipitation changes. Changes in neither the wind stress strength nor its position are directly linked to the ACC transport changes.

The influence of winds on the ACC and MOC can be investigated by isolating 1) the influence of increased wind strength and 2) the combined influence of an increased strength and a poleward shift in the winds [the latter being closer to most future climate predictions; e.g., Sen Gupta et al. (2009)]. Coarse-resolution coupled climate model studies where solely the wind strength is perturbed by 20%–50%, but the latitudinal position remains constant, show that the ACC changes by less than 10% (e.g., Gent and Danabasoglu 2011). On the other hand, when a strengthening of the winds is accompanied by a poleward migration, studies have shown significant increases in the ACC transport (more than 30%) and the steepening of associated isopycnals (Gent and Danabasoglu 2011; Farneti et al. 2010; Farneti and Gent 2011). Here, 4 of the 13 models assessed show no shift in the wind stress position under RCP8.5 forcing (Fig. 1d); however, the absence of a meridional shift does not correspond with smaller ACC transport changes.

We assessed the role of wind and buoyancy forcing on the four models that outputted MOC in density space for the 1950–2100 period (also under RCP8.5 forcing). The strengthened zonal wind stress drives an equatorward flow in the Ekman layer, as well as increasing the downwelling of water masses and thus strengthening the upper MOC cells. In the models where the winds shift poleward significantly (models 5 and 7), the combined increases in wind stress and surface warming (due to increased input of air–sea surface heat fluxes) increase the strength of the eddy lower MOC cell. The opposite occurs in the models where the change in the latitude of the wind stress maximum is minimal (models 1 and 2).

In previous studies where the response of the ACC transport to increased winds has been assessed in both high- and coarse-resolution models, the high-resolution models imply an eddy saturated state while the coarse-resolution models exhibit greater sensitivity in ACC transport (e.g., Meredith et al. 2012; Farneti and Gent 2011; Farneti et al. 2010; Munday et al. 2013). Here, where both buoyancy and wind respond to an extreme climate scenario, the wind stress changes by no more than ~20%; these changes are not correlated with ACC transport projections. Warming in the southern ACC region and freshening (possibly associated with a poleward shift in the westerlies) that acts to flatten and deepen isopycnals are associated with a weaker ACC transport.

We suggest that the results presented here may be interpreted in one of three ways. One possibility is that parameterized eddies in coarse-resolution models do a good job of representing the eddy saturation regime expected in higher-resolution models. If so, then the ACC transport changes noted here represent an accurate future pathway. Alternatively, it is possible that these models are sensitive to wind stress changes but that wind-driven increases in the ACC transport are offset by changes in the surface buoyancy forcing. In this case, it is reasonable to suggest that an eddy-resolving model would predict weaker ACC transport changes

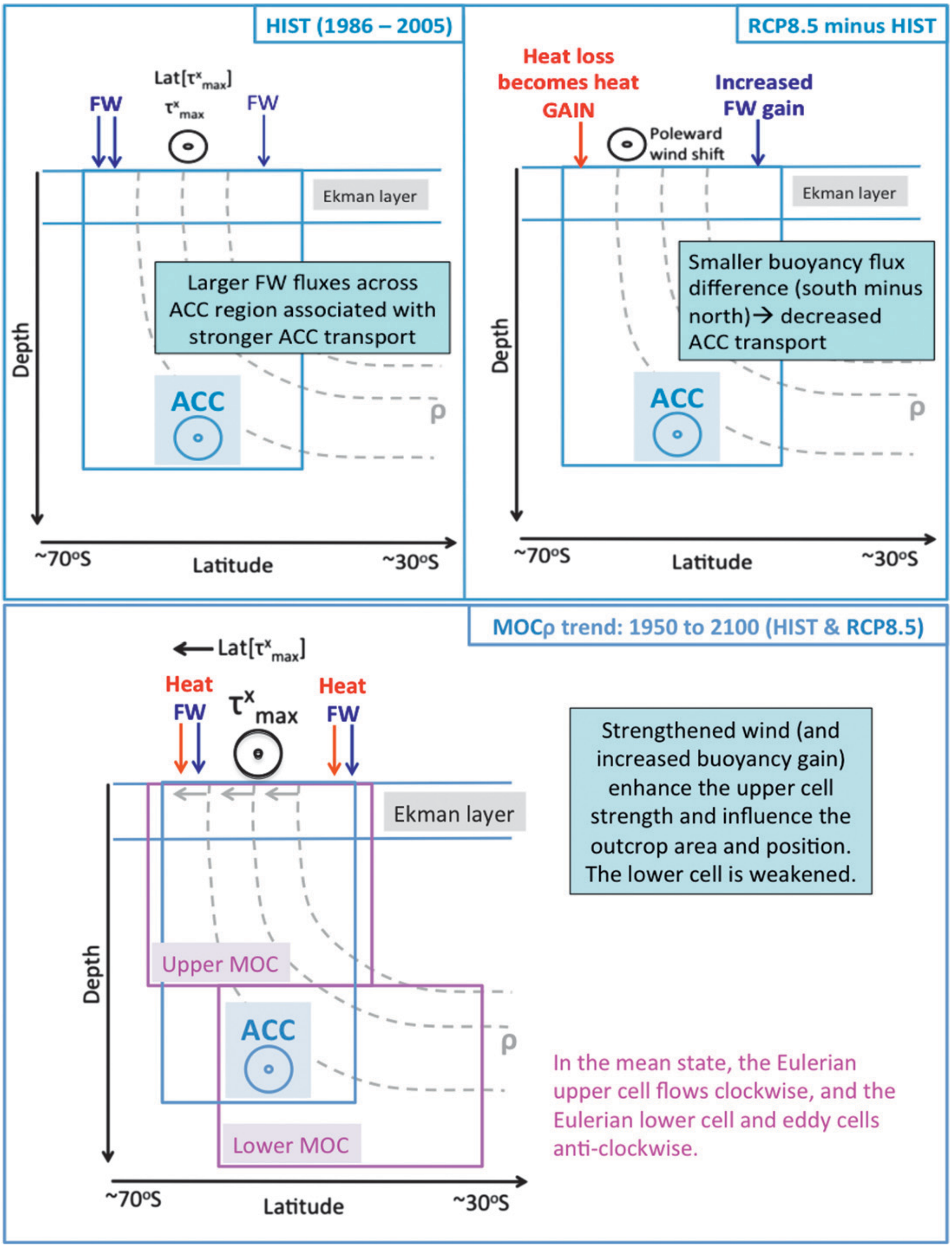

FIG. 12. Summary of ACC results for the (top left) HIST period and (top right) time difference (RCP8.5 − HIST) for 13 CMIP5 models. Illustrated are the main components of the zonal-mean Southern Ocean circulation, including the eastward-flowing ACC with gray dashed curves representing isopycnals (ρ). Heat and FW input into the ocean surface (i.e., a buoyancy gain) are represented by red and blue arrows, respectively. Also shown are the eastward-flowing zonal-mean zonal-wind stress maximum ($\tau^x_{\max}$) and the latitude of this maximum (lat[$\tau^x_{\max}$]). (bottom) The trends for the wind and buoyancy fluxes influencing MOC in density space (MOCρ) for the 1950–2100 period (HIST and RCP8.5 experiments combined). The upper and lower overturning cells are bounded by the magenta boxes. An interpretation of our main results for the ACC transport and MOCρ are summarized in the blue boxes with black text.

under future climate scenarios. The third possibility is that the wind changes are too low to produce a significant ACC response. This study cannot distinguish between these scenarios but does suggest that the topic warrants further investigation.

The eddy MOC cell primarily compensates the lower Eulerian cell in density space and the upper Eulerian cell in depth space; hence, the two coordinate frameworks quantitatively present differing conclusions. We found that four of the eight models indicated eddy compensation under RCP8.5 forcing for the upper cell in depth space and one for the lower cell. However, at best the models show partial eddy compensation in density space where the Eulerian cell changes were larger than those in the eddy cells.

In terms of linking the MOC in density space and ACC transport (in models 1, 2, 5, and 7), we find that ACCESS1.3 (model 2) has the strongest ACC transport and MOC cell strength in the HIST period with strong (but not the strongest) wind stress (Figs. 1, 9). Under RCP8.5 forcing, the ACCESS1.3 model also exhibits the strongest ACC change (decrease) and the largest change in the lower Eulerian MOC cell, combined with strong warming south of the wind stress maximum. The wind stress maximum does not shift and the wind stress increases minimally. Warming of southern surface waters reduces the density gradient across the ACC region. This combined with isopycnal flattening south of 55°S in the ACCESS1.3 model (Fig. 5) is associated with a weakening of the ACC. The minimal shift and strengthening of winds compared with the other three models would result in small changes in upwelling that influences the lower cell overturning decrease. We do not find a similar result for the other three models; however, in this model at least the ACC and MOC may be tightly linked.

One would assume that it is difficult to draw nonbiased conclusions on the quantitative aspects of the overturning circulation, given that three of the four models used in the eddy compensation section utilize the same ocean component (MOM4p1; Griffies 2007). On the other hand, it is clear from our results that the three MOM4p1-based models (ACCESS1.0, ACCESS1.3, and ESM2M) have distinct atmospheric, land, and sea ice components (cf. model numbers 1, 2, and 5 in Figs. 1, 2) that produce differing MOC cell strengths and changes (Figs. 7, 8). In addition, it is interesting that these three models show a similar relationship between the 150-yr trend in the MOC cells and surface forcing (Table 2). In short, we regard having three models with the same ocean as a benefit in highlighting the strong relationship between large-scale circulation and surface wind and buoyancy fluxes.

On a similar note, it would be prudent to compare the results of the two CAWCR models with the same ocean but different atmosphere (ACCESS1.0 and ACCESS1.3; model numbers 1 and 2) and the two GFDL models with different oceans but the same atmosphere (ESM2M and ESM2G; model numbers 5 and 10). We find that the ACCESS models differ substantially in their wind stress, ACC transport, and buoyancy-forcing trends under RCP8.5 forcing. The two GFDL models (ESM2M and ESM2G) have very similar mean and varied surface buoyancy fluxes, wind strength, and position; there is a slighter larger heat gain north of the wind stress maximum in ESM2M. The ACC transport in both models appears insensitive to the large changes in surface winds; however, the isopycnal depth increases throughout the water column. These findings suggest that models with differing atmospheres have different oceanic responses to climate forcing, whereas models with the same atmospheric component and differing oceans will respond similarly. That is, the atmospheric model component is important in the study of the oceanic response to climate change.

Our analysis of the 13 CMIP5 models has generated numerous points of discussion regarding model ensembles and model drift. We have chosen the first ensemble member (r1i1p1) uniformly across all models for both the HIST and RCP8.5 experiment. For the latter experiment, the r1i1p1 ensemble member is primarily the only one available. For the HIST experiment many models output numerous ensemble members; however, some only output just one. Quantifying how our results would differ if we were to average multiple ensemble members per model is beyond the scope of this study, though we regard it as an important avenue for future investigation.

We have not subtracted drift in our results from, in particular, model fields initialized using observations such as temperature, salinity, and density. Previous studies have highlighted significant model drift in the CMIP3 models. For example, Sloyan and Kamenkovich (2007) noted up to 0.6°C temperature and 0.1 psu salinity drift over a 100-yr period in the eight CMIP3 models they analyzed. Sen Gupta et al. (2009) concluded that the temperature drift in many of the 16 CMIP3 models they analyzed was of a similar order of magnitude to the twenty-first-century trend. We note that model drift estimated spatially along depth or density surfaces is likely to differ from a zonal-mean framework, and this needs to be quantitatively assessed in future model analyses. We argue that removing model drift from our results would not alter our main conclusions based on two premises. First, many of the CMIP5 models have a smaller model drift compared with their CMIP3 versions (Voldoire et al. 2013; Rotstayn et al. 2012; Yukimoto

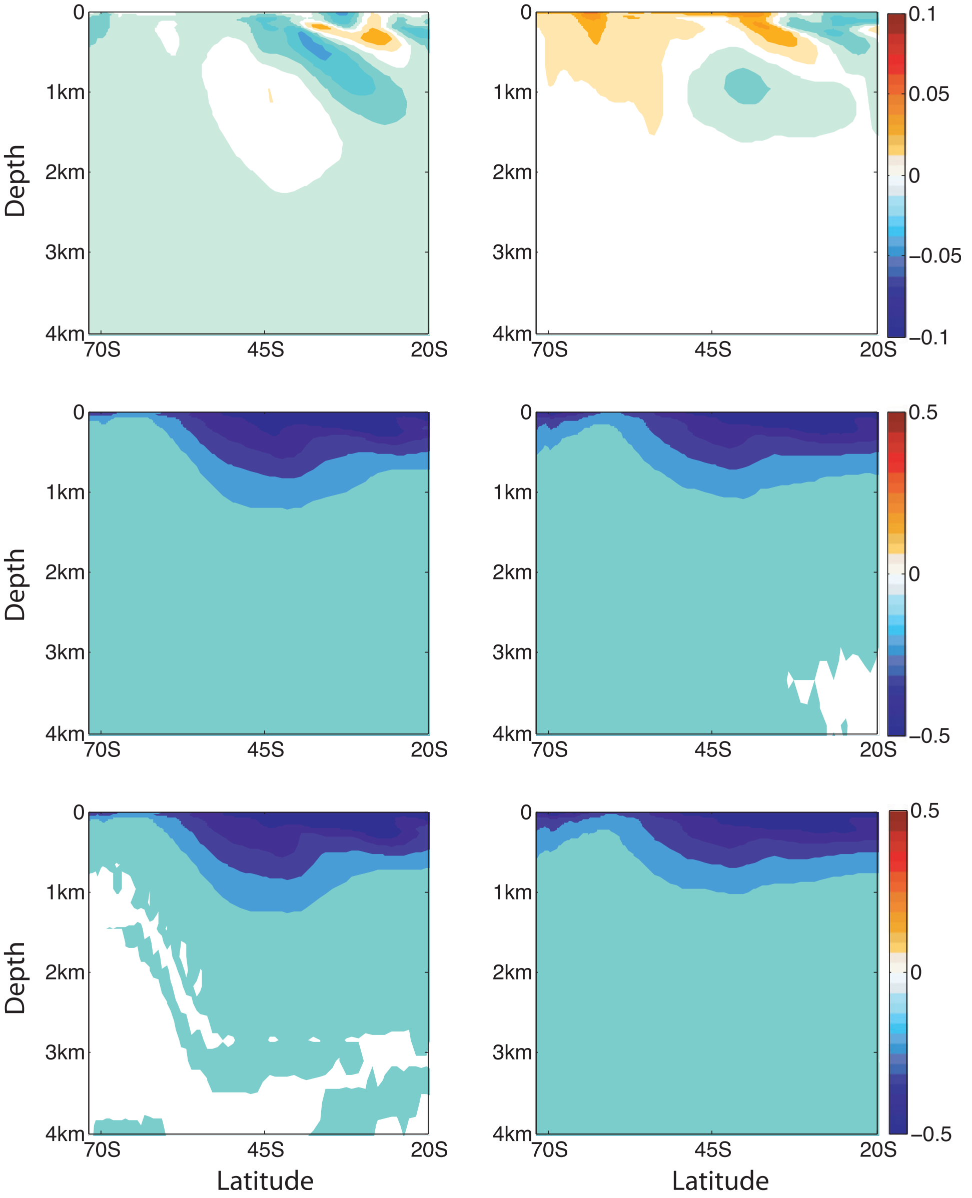

FIG. 13. Zonal-mean density in models (left) ACCESS1.0 and (right) ACCESS1.3 (kg m^{-3}). (top) The 100-yr trend over the twenty-first century for the preindustrial control experiment (i.e., with no present day, historical, or future forcing). (middle) The density difference between the RCP8.5 and HIST experiments. (bottom) As in (middle), but with the linear trend in the first row subtracted.

et al. 2012). Second, we estimated the model drift in 4 of the 13 models assessed (results from the ACCESS models are shown in Fig. 13) and found the drift to be small in comparison to the twenty-first-century trend in the upper 2 km. Below this depth, the density trend and model drift are minimal (<0.1 kg m^{-3}) and of similar magnitude in some regions. We conclude that the regions of largest density change in response to the large radiation changes imposed by the RCP8.5 experiment are only weakly affected by model drift.

5. Conclusions

We have presented multimodel results of changes in the ACC transport and overturning circulation under the RCP8.5 experiment using a suite of CMIP5 models. We have focused on the influence of eddy fluxes, winds, and surface buoyancy fluxes. We identify the following robust CMIP5 model responses from our study:

1) In the RCP8.5 experiment, the ACC transport changes across the 13 CMIP5 models are uncorrelated with

wind stress. However, the wind stress changes are moderate when compared with previous wind perturbation studies, and surface buoyancy fluxes play a dominant role in compensating wind stress influences in these coupled climate simulations.

2) The four models used to analyze responses in MOC cells in density space project a strong correlation between increased upper and decreased lower Eulerian MOC cells and the wind-driven transports and heat gain across the ACC region. This result is contrary to the ACC transport response, which shows a weak relationship with wind stress changes.
3) These models project partial eddy compensation of the upper MOC cell. Full compensation is unlikely to be achieved with the weak eddy responses and strong correlations with surface buoyancy changes (and it is not found in eddy-resolving models in any case).
4) Surface buoyancy fluxes clearly influence the ACC transport, as does the choice of the atmospheric, land, and sea ice components coupled to the ocean models.

A more uniform conclusion regarding eddies and overturning requires both an evaluation of more CMIP5 models or of fewer models with varied forcing (e.g., isolating volcanic or greenhouse gas forcing). Given the significant magnitude of eddy overturning in the mean state and its significant future role in enhancing the upper and reducing the lower Southern Ocean meridional overturning circulation, we suggest that there is an urgent need for more modeling groups to consider archiving the overturning circulation in density space and including eddy contributions in future CMIP efforts.

Acknowledgments. The authors wish to thank the modelers responsible for the development of the CMIP5 models analyzed here and their continuous assistance with these types of multimodel projects. We are grateful for the constructive comments provided by A. Gnanadesikan and three anonymous reviewers. This research was undertaken on the NCI National Facility in Canberra, Australia, which is supported by the Australian Commonwealth Government. We are grateful for the efforts of particular Paola Petrelli for improving access to CMIP5 output. AMH was supported by an Australian Research Council Future Fellowship FT120100842.

REFERENCES

Bao, Q., and Coauthors, 2013: The Flexible Global Ocean-Atmosphere-Land System Model, spectral version 2: FGOALS-s2. *Adv. Atmos. Sci.,* **30,** 561–576.

Bi, D., and S. Marsland, 2010: Australian Climate Ocean Model (AusCOM) users guide. CAWCR Tech. Rep. 027, 72 pp.

——, and Coauthors, 2013: The ACCESS coupled model: Description, control climate and evaluation. *Aust. Meteor. Oceanogr. J.,* in press.

Borowski, D., R. Gerdes, and D. Olbers, 2002: Thermohaline and wind forcing of a circumpolar channel with blocked geostrophic contours. *J. Phys. Oceanogr.,* **32,** 2520–2540.

Chylek, P., J. Li, M. K. Dubey, M. Wang, and G. Lesins, 2011: Observed and model simulated 20th century Arctic temperature variability: Canadian Earth System Model CANESM2. *Atmos. Chem. Phys. Discuss.,* **11,** 22 893–22 907, doi:10.5194/acpd-11-22893-2011.

Collins, W., and Coauthors, 2008: Evaluation of the HADGEM2 model. Met Office Hadley Centre Tech. Note 74, 47 pp.

Cunningham, S. A., S. G. Alderson, B. A. King, and M. A. Brandon, 2003: Transport and variability of the Antarctic Circumpolar Current in Drake Passage. *J. Geophys. Res.,* **108,** 8084, doi:10.1029/2001JC001147.

Downes, S. M., N. L. Bindoff, and S. R. Rintoul, 2010: Changes in the subduction of Southern Ocean water masses at the end of the twenty-first century in eight IPCC models. *J. Climate,* **23,** 6526–6541.

——, A. Gnanadesikan, S. M. Griffies, and J. L. Sarmiento, 2011: Water mass exchange in the Southern Ocean in coupled climate models. *J. Phys. Oceanogr.,* **41,** 1756–1771.

Dunne, J. P., and Coauthors, 2012: GFDL's ESM2 global coupled climate–carbon earth system models. Part I: Physical formulation and baseline simulation characteristics. *J. Climate,* **25,** 6646–6665.

Essery, R., M. Best, and P. Cox, 2001: Moses 2.2 technical documentation. Hadley Centre Tech. Note 30, 30 pp.

Farneti, R., and P. Gent, 2011: The effects of the eddy-induced advection coefficient in a coarse-resolution coupled climate model. *Ocean Modell.,* **39,** 135–145.

——, T. L. Delworth, A. J. Rosati, S. M. Griffies, and F. Zeng, 2010: The role of mesoscale eddies in the rectification of the Southern Ocean response to climate change. *J. Phys. Oceanogr.,* **40,** 1539–1557.

Fyfe, J. C., and O. A. Saenko, 2006: Simulated changes in the extratropical Southern Hemisphere winds and currents. *Geophys. Res. Lett.,* **33,** L06701, doi:10.1029/2005GL025332.

Gent, P. R., and J. C. McWilliams, 1990: Isopycnal mixing in ocean circulation models. *J. Phys. Oceanogr.,* **20,** 150–155.

——, and G. Danabasoglu, 2011: Response to increasing Southern Hemisphere winds in CCSM4. *J. Climate,* **24,** 4992–4998.

——, and Coauthors, 2011: The Community Climate System Model version 4. *J. Climate,* **24,** 4973–4991.

Griesel, A., M. R. Mazloff, and S. T. Gille, 2012: Mean dynamic topography in the Southern Ocean: Evaluating Antarctic Circumpolar Current transport. *J. Geophys. Res.,* **117,** C01020, doi:10.1029/2011JC007573.

Griffies, S. M., 1998: The Gent–McWilliams skew flux. *J. Phys. Oceanogr.,* **28,** 831–841.

——, 2007: Elements of MOM4p1. GFDL Ocean Group Tech. Rep. 6, 446 pp.

——, 2012: Elements of the Modular Ocean Model (MOM): 2012 release. GFDL Ocean Group Tech. Rep. 7, 618 pp.

——, and Coauthors, 2011: The GFDL CM3 coupled climate model: Characteristics of the ocean and sea ice simulations. *J. Climate,* **24,** 3520–3544.

Hallberg, R. W., and A. Gnanadesikan, 2006: The role of eddies in determining the structure and response of the wind-driven Southern Hemisphere overturning: Results from the Modeling Eddies in the Southern Ocean (MESO) Project. *J. Phys. Oceanogr.,* **36,** 2232–2252.

Hewitt, H. T., D. Copsey, I. D. Culverwell, C. M. Harris, R. S. R. Hill, A. B. Keen, A. J. McLaren, and E. C. Hunke, 2011: Design and implementation of the infrastructure of HadGEM3: The next-generation Met Office climate modelling system. *Geosci. Model Dev. Discuss.,* **4,** 223–253.

Hogg, A. M., 2010: An Antarctic Circumpolar Current driven by surface buoyancy forcing. *Geophys. Res. Lett.,* **37,** L23601, doi:10.1029/2010GL044777.

Kuhlbrodt, T., R. Smith, Z. Wang, and J. Gregory, 2012: The influence of eddy parameterizations on the transport of the Antarctic Circumpolar Current in coupled climate models. *Ocean. Modell.,* **52–53,** 1–8, doi:10.1016/j.ocemod.2012.04.006.

Large, W., and S. Yeager, 2009: The global climatology of an interannually varying air–sea flux data set. *Climate Dyn.,* **33,** 341–364, doi:10.1007/s00382-008-0441-3.

Le Quéré, C., and Coauthors, 2007: Saturation of the Southern Ocean CO_2 sink due to recent climate change. *Science,* **316,** 1735–1738.

Lumpkin, R., and K. Speer, 2007: Global ocean meridional overturning. *J. Phys. Oceanogr.,* **37,** 2550–2562.

Marshall, J., and T. Radko, 2003: Residual-mean solutions for the Antarctic Circumpolar Current and its associated overturning circulation. *J. Phys. Oceanogr.,* **33,** 2341–2354.

Meredith, M. P., A. C. Naveira-Garabato, A. M. Hogg, and R. Farneti, 2012: Sensitivity of the overturning circulation in the Southern Ocean to decadal changes in wind forcing. *J. Climate,* **25,** 99–110.

Morrison, A. K., and A. M. Hogg, 2013: On the relationship between Southern Ocean overturning and ACC transport. *J. Phys. Oceanogr.,* **43,** 140–148.

——, ——, and M. L. Ward, 2011: Sensitivity of the Southern Ocean overturning circulation to surface buoyancy forcing. *Geophys. Res. Lett.,* **38,** L14602, doi:10.1029/2011GL048031.

Moss, R. H., and Coauthors, 2010: The next generation of scenarios for climate change research and assessment. *Nature,* **463,** 747–756.

Munday, D. R., H. L. Johnson, and D. P. Marshall, 2013: Eddy saturation of equilibrated circumpolar currents. *J. Phys. Oceanogr.,* **43,** 507–532.

Ridgway, K., J. Dunn, and J. Wilkin, 2002: Ocean interpolation by four-dimensional least squares—Application to the waters around Australia. *J. Atmos. Oceanic Technol.,* **19,** 1357–1375.

Rintoul, S. R., C. W. Hughes, and D. Olbers, 2001: The Antarctic circumpolar system. *Ocean Circulation and Climate,* G. Siedler et al., Eds., Academic Press, 271–302.

Rotstayn, L. D., S. J. Jeffrey, M. A. Collier, S. M. Dravitzki, A. C. Hirst, J. I. Syktus, and K. K. Wong, 2012: Aerosol-induced changes in summer rainfall and circulation in the Australasian region: A study using single-forcing climate simulations. *Atmos. Chem. Phys. Discuss.,* **12,** 5107–5188, doi:10.5194/acpd-12-5107-2012.

Sabine, C. L., and Coauthors, 2004: The oceanic sink for anthropogenic CO_2. *Science,* **305,** 367–371.

Schmidt, G. A., and Coauthors, 2006: Present-day atmospheric simulations using GISS modelE: Comparison to in situ, satellite, and reanalysis data. *J. Climate,* **19,** 153–192.

Sen Gupta, A., A. Santoso, A. S. Taschetto, C. C. Ummenhofer, J. Trevena, and M. H. England, 2009: Projected changes to the Southern Hemisphere ocean and sea ice in the IPCC AR4 climate models. *J. Climate,* **22,** 3047–3078.

Shakespeare, C. J., and A. M. Hogg, 2012: An analytical model of the response of the meridional overturning circulation to changes in wind and buoyancy forcing. *J. Phys. Oceanogr.,* **42,** 1270–1287.

Sloyan, B. M., and S. R. Rintoul, 2001: The Southern Ocean limb of the global deep overturning circulation. *J. Phys. Oceanogr.,* **31,** 143–173.

——, and I. V. Kamenkovich, 2007: Simulation of Subantarctic Mode Water and Antarctic Intermediate Water in climate models. *J. Climate,* **20,** 5061–5080.

Smith, R. N. B., 1990: A scheme for predicting layer clouds and their water content in a general circulation model. *Quart. J. Roy. Meteor. Soc.,* **116,** 435–460, doi:10.1002/qj.49711649210.

Speer, K., S. R. Rintoul, and B. Sloyan, 2000: The diabatic Deacon cell. *J. Phys. Oceanogr.,* **30,** 3212–3222.

Straub, D. N., 1993: On the transport and angular momentum balance of channel models of the Antarctic Circumpolar Current. *J. Phys. Oceanogr.,* **23,** 776–782.

Swart, N. C., and J. C. Fyfe, 2012: Observed and simulated changes in the Southern Hemisphere surface westerly wind-stress. *Geophys. Res. Lett.,* **39,** L16711, doi:10.1029/2012GL052810.

Taylor, K. E., R. J. Stouffer, and G. A. Meehl, 2012: An overview of CMIP5 and the experiment design. *Bull. Amer. Meteor. Soc.,* **93,** 485–498.

Viebahn, J., and C. Eden, 2010: Towards the impact of eddies on the response of the Southern Ocean to climate change. *Ocean Modell.,* **34,** 150–165.

Voldoire, A., and Coauthors, 2013: The CNRM-CM5.1 global climate model: Description and basic evaluation. *Climate Dyn.,* **40,** 1–31, doi:10.1007/s00382-011-1259-y.

Wang, Z., T. Kuhlbrodt, and M. P. Meredith, 2011: On the response of the Antarctic Circumpolar Current transport to climate change in coupled climate models. *J. Geophys. Res.,* **116,** C08011, doi:10.1029/2010JC006757.

Wilson, D. R., A. C. Bushell, A. M. Kerr-Munslow, J. D. Price, and C. J. Morcrette, 2008: PC2: A prognostic cloud fraction and condensation scheme. I: Scheme description. *Quart. J. Roy. Meteor. Soc.,* **134,** 2093–2107.

Yukimoto, S., and Coauthors, 2012: A new global climate model of the meteorological research institute: MRI-CGCM3—Model description and basic performance. *J. Meteor. Soc. Japan,* **90A,** 23–64.